ABSTRACT

Title of dissertation: COMPLEX DYNAMICS
OF A MICROWAVE
TIME-DELAYED FEEDBACK LOOP

Hien Thi Le Dao, Doctor of Philosophy, 2013

Dissertation directed by: Professor Thomas E. Murphy
Department of Electrical & Computer Engineering

The subject of this thesis is deterministic behaviors generated from a microwave time-delayed feedback loop. Time-delayed feedback systems are especially interesting because of the rich variety of dynamical behaviors that they can support. While ordinary differential equations must be of at least third-order to produce chaos, even a simple first-order nonlinear delay differential equation can produce higher-dimensional chaotic dynamics. The system reported in the thesis is governed by a very simple nonlinear delay differential equation. The experimental implementation uses both microwave and digital components to achieve the nonlinearity and time-delayed feedback, respectively. When a sinusoidal nonlinearity is incorporated, the dynamical behaviors range from fixed-point to periodic to chaotic depending on the feedback strength. The microwave frequency modulated chaotic signal generated by this system offers advantages in range and velocity sensing applications. When the sinusoidal nonlinearity is replaced by a binary nonlinearity, the system exhibits a complex periodic attractor with no fixed-point solution. Although there are many

classic electronic circuits that produce chaotic behavior, microwave sources of chaos are especially relevant in communication and sensing applications where the signal must be transmitted between locations. The system also can exhibit random walk behavior when being operated in a higher feedback strength regime. Depending on the feedback strength values, the random behaviors can have properties of a regular or fractional Brownian motion. By unidirectional coupling two systems in the base-band, envelope synchronization between two deterministic Brownian motions can be achieved.

COMPLEX DYNAMICS OF A MICROWAVE TIME-DELAYED FEEDBACK LOOP

by

Hien Thi Le Dao

Dissertation submitted to the Faculty of the Graduate School of the
University of Maryland, College Park in partial fulfillment
of the requirements for the degree of
Doctor of Philosophy
2013

Advisory Committee:
Professor Thomas E. Murphy, Chair/Advisor
Professor Rajarshi Roy, Co-Advisor
Dr. John C. Rodgers, Co-Advisor
Professor Brian R. Hunt
Professor Michelle Girvan

We have to continue to learn. We have to be open. And we have to be ready to release our knowledge in order to come to a higher understanding of reality.

- Thich Nhat Hanh.

Dedication

To my father

Acknowledgments

It is impossible to list all the people who have helped me during this academic journey. Their advice, friendship, and encouragement have shaped my life in ways I could never imagine.

I would like to express my most sincere gratitude to my PhD advisors- Professor Thomas E. Murphy, Professor Rajarshi Roy and Dr. John Rodgers- for their tremendous guidance and support. I thank Raj for introducing me to the world of nonlinear science research. His wise suggestions and comments always stood out and helped to move the projects in the best direction. I am very grateful to work with John, who has transformed me from a physics theorist to a chaos experimentalist with his knowledge about microwave devices and technical instruments. I deeply appreciate his guidance on setting up the experimental system, and his advice on recording data. I am indebted to Tom for his fundamental role on my doctoral work. Tom had worked with me closely on all the projects. He provided me advice, assistance and support that I needed toward the completion of this thesis. The expertise in scientific writing, presentation and image editing that I have learned from Tom is immensely valuable. In addition to our academic collaboration, his understanding and thoughtfulness on my personal situation have helped me persevere through various stages of the process. I simply cannot ask for a better mentor.

I thank Professor Brian R. Hunt and Professor Michelle Girvan for kindly agreeing to serve on my advisory committee. I would like to greatly acknowledge their insightful comments and valuable suggestions.

I also thank Professor Michael Coplan, Debbie Jenkins and other faculty members in the Chemical Physics Program. Their support during my graduate study has helped me make significant progress with my research. I particularly appreciate regular meetings with Professor Coplan on my academic performance. His course on research electronics has substantially influenced my research.

I would like to thank Jay Pyle for his help on the machine shop. I appreciate the work of other IREAP staffs to smooth out works beyond research: Edward Condon for his assistance in computer network, Nancy Boone for devices purchasing, Dorothea Brosius for the thesis template, and Margaret Hass and Leslie Delabar for providing the lactation room.

I appreciate the work of Kathryn Tracey, Mohini Kaul, and Denise M. Abu-Laban on conference registration and reimbursement.

I have been fortunate to have scientific and personal interactions with Adam B. Cohen, Bhargava Ravoori, Caitlin Williams and Aaron Hagestrom. Adam and Bhargava have offered me great comments and suggestions on my work since the beginning. My friendship with Caitlin helped me endure tough moments in graduate school. I appreciate Aaron's comments on my writing.

Finally, I am deeply blessed for my family. There is no word to convey how much I love and appreciate them. My parents, Dr. Hoan V. Dao and Mrs. Luu Le, have always been a great inspiration on the study of physics. Their attitude about education have shaped my life in fundamental ways. I thank my sisters, Hue Dao and Thanh Dao, for being my best friends. I appreciate Hue for taking over the responsibility of the oldest daughter while I was away. Weekly conversations

with Hue and Thanh helped me to stay committed and focused during the past five years.

I met and married my husband, Tam Huynh, during my time of doctoral work. I am thankful for being with such a loving, considerate, and responsible man. During my hard times with schoolwork, Tam always stays by my side with uncountable encouragements. He is my true and great supporter who has never lost faith in me. I am blessed with our beautiful son, William Huynh who now is an expert of making chaos in the house. I am looking forward to spend my unpredictable future with these two wonderful guys.

The last five years have been the most exciting journey for me, both academically and personally. I am thankful for all the interactions that have helped me become who I am today.

Table of Contents

List of Tables

List of Figures

Chapter 1: Introduction

1.1 Deterministic Chaos

With the appearance of differential equations, the three laws of motion and universal gravitation discovered by Newton in the mid -1600s, dynamics has become the most active research branch in physics and mathematics. The basic problem of dynamics is to predict the future state of a system given the system's initial state. The system under consideration maybe physical, chemical, or biochemical. Regardless of the context, many systems are modeled mathematically as differential equations with time as a continuous variable, or as difference equations where time will take on discrete integer values. Systems described by deterministic evolution equations are called deterministic dynamical systems. A basic problem in astronomy, the three-body gravitational system, in 1887 challenged the understanding of scientists when they could not demonstrate the stability or any orbit of the Solar system. A two hundred page paper written by the mathematician H. Poincaré showed that the problem is "impossible to solve because it may happen that small differences in the initial conditions produce very great ones in the final state. Prediction (of the future states) becomes impossible" [1]. The phenomenon Poincaré discovered was an initial anticipation of modern deterministic chaos. However, this

discovery wasn't widely appreciated by the scientific society at the time because the mathematical works were difficult to read; and the theories weren't explicit and general enough to convince scientists about the universality of chaos. This deterministic aperiodic behavior therefore remained in the background as a curiosity of dynamical systems for the next 70 years, until high speed computers were invented in the 1950s and gave scientists like the meteorologist E. N. Lorenz opportunities to work with differential equations in a way that was never possible before. While working on modeling the weather system, Lorenz discovered that a set of three first order, coupled and nonlinear differential equations could display solutions in which the trajectories could be strongly divergent if the simulation is started from slightly different initial conditions [2]. This property is illustrated in the solutions of the equations which never settle down to an equilibrium or periodic state; instead the solution continues to oscillate in an aperiodic fashion. Lorenz's works provided the strong foundations for chaos theory in the 1970s when the speed of computers improved and refined experimental techniques were developed. With discovery after discovery, it has come clear that chaos is ubiquitous in nature and could appear in most branches of science [3]. Besides the known examples of the Solar and weather systems, chaos could be seen in turbulent fluids [4, 5], the motion of electrons in atoms [6], and population dynamics in biology [7].

The uniqueness and universality of chaos can bring out its relevance to a lot of applications besides the interest in fundamental scientific problems. To name a few, the complex and noise-like characteristics of chaotic signals could have advantages in a variety of practical applications. Chaotic signals have been proposed to

reduce interference and cross-talk in diverse contexts, including wireless networks, sonar networks, fiber-optic links, and electric power systems [8–11]. Chaotic modulation methods have been used to encrypt or mask information in communication systems [12–14]. The unpredictability of chaotic signals has been exploited for high-speed random number generation [15–19]. Chaotic signals often exhibit a wide spectral bandwidth and a short correlation time, which is useful for increasing the precision of range and velocity detection in radar, lidar and sonar systems [20–23]. Some of the promising applications of chaos in biology involve complicated systems whose underlying laws are not well defined. The hope is that the erratic dynamics of these systems may be consequences of the deterministic chaos governed by nonlinear equations such as the model of blood production of Mackey and Glass [24] in leukemia patients.

1.2 Delay Differential Equations

The wide range of possible applications of chaos raise the interest in generating strong and well-controlled chaotic dynamics. When one seeks ways to create chaotic behaviors, a natural question to ask is: where is chaos coming from? And what are the requirements for a dynamical system to exhibit such complicated behavior? Analyzing the Lorenz equations, one can see that the deterministic chaotic behavior is neither due to external sources of noise (there are none in the equations) nor to an infinite number of degrees of freedom (there are only three degrees of freedom in the equations), nor the uncertainty associated with quantum mechanics (the

equation are purely classical). The erratic behavior exhibited by the Lorenz system is instead due to properties often seen in the nonlinear systems. These include exponentially fast separating initially close trajectories in a bounded region of phase space [25]. However, nonlinearity is a necessary but not a sufficient condition for the generation of chaotic motion since linear differential or difference equations can be solved by Fourier transformation and they do not lead to chaos. For a dynamical system governed by a set of N first order autonomous, coupled, nonlinear, ordinary differential equations (ODE), it is known that N must be equal or greater than three for chaos to be possible [26]. Now, there remains the problem of describing systems in terms of a series of ODEs to check the possibility of aperiodic behaviors. For any system described by one or more nonlinear delay differential equations (DDEs), chaos is possible. Delay differential equations are a different class of equations in which the solution depends not only on the initial state but the state of the system over some time interval. This type of differential equation was developed and intensively studied after the First World War due to the high demand for automatic control systems. The time delay arises because one cannot ignore the propagation time of signals in the control systems in comparison to the time-scale of the system dynamics. One can therefore find DDEs as the mathematical description of feedback systems with non-negligible delay times.

The solution of a DDE is determined not only by its initial state but the whole solution profile of the system on a given interval equal to the delay time. Therefore, to solve a DDE, one must provide not just the state of the system at the initial point but the history which is the solution over an interval prior to the initial point

i.e., one must define an infinite-dimensional set of initial conditions. Thus DDEs are inherently infinite-dimensional equations even if we only have one single linear DDE. Because of this unique property, DDEs could have a long-time oscillatory solution; also the short-time solutions might be affected due to the propagation of discontinuities [27]. There are several analytical methods available to solve DDEs although most of the time solutions are approximated using numerical techniques. The first and most popular method is perturbation in terms of a small or large limit of control parameters. One can also use the linear stability technique [28, 29], or multiple time-scale methods [30]. The results are often presented as a bifurcation diagram where a property of the solution is recorded as a function of a control parameter.

DDEs have played an important role in modeling population dynamics with their inherent maturation and gestation time delays [31]. DDEs also have been used extensively to study traffic flow with the car- following model in which the location and the speed of the following car is determined by the speed pattern of leading vehicles [32]. One can derive a DDE to model problems in nonlinear optics [33–35], fluid dynamics [36,37], mechanical engineering [38–40], epidemics [41], economics [42](time delay coming from the lag between the investment decision and installation of investment goods) and in radio-frequency (RF) communication systems since the time it takes signals to propagate through many RF devices is comparable to the time scale of dynamics. In electrical engineering, one can use DDEs to describe nonlinear time-delayed feedback loops which contain a passive nonlinear element, an amplifier for gain, a loop delay and band-limited feedback.

This architecture has been an effective method to generate chaos using a combination of optical and electronic components [43–45]. The chaotic signals generated by these systems are examples of *amplitude chaos*, i.e., a signal with an irregular time-varying amplitude or envelope. However, for some applications in communication, it is preferable to use *phase chaos*, in which the chaotic RF signal has a constant amplitude and a chaotic phase or frequency. Within the framework of this thesis, we will apply the architecture on a frequency modulated microwave loop to study chaos and associated dynamical behaviors.

1.3 Microwave Signals

In 1873, the existence of electromagnetic waves was predicted by J. C. Maxwell [46] using his equations for electric and magnetic fields with the implication that light was a form of electromagnetic energy. His work, after being modified by the vector notation of O. Heaviside, was tested by a well-known experiment conducted by H. Hertz. Signals with frequencies as high as 450 MHz were generated from the spark gap radio transmitter in 1888 as the first demonstration of microwaves [47]. From then on, the term microwave was reserved for the signals whose frequencies range from 300 MHz to 300 GHz, with a corresponding electrical wavelength from 1m to 1 mm. In electromagnetic and circuit theory, this term has more technical meaning. Generally speaking, a system or any apparatus might be described qualitatively as microwave when the frequencies are high enough that the wavelengths are short and roughly the same as the physical dimension of devices. Therefore most microwave

components are distributed elements and transmission-line theory is used to analyze microwave circuits instead of the lumped-element circuit theory.

Although short wavelengths can cause difficulty in the analysis and design microwave components, this factor also provides opportunities for the application of microwave signals. Since most of molecular, atomic and nuclear resonance phenomena occur at high frequencies, studying microwaves helps to create unique applications in basic sciences, medical treatment and diagnostics, remote sensing and heating methods [48, 49]. The majority of microwave applications are related to radar and communication systems. Radar technology was developed intensively during the Second World War due to its great military utility in locating targets. Microwave signals are used in radar systems to detect the range and speed of remote projects because it produces more antenna gain at higher frequencies for a given antenna physical size; it also increases the effective reflection area (i.e., radar cross section) for a given target's electrical size. Modern radar systems have been used not only in military applications but for traffic- control, missile tracking, automobile collision avoidance, weather prediction, and a wide variety of remote sensing applications [49,50]. Communication systems using microwave technology were also developed soon after the birth of radar. The fact that more bandwidth can be realized at higher frequencies helps to have a larger capacity for information- carrying signals in communication in comparison to radio frequencies. Moreover, microwave signals travel with the speed of light and are not bent by the Earth's ionosphere as are the lower frequencies signals, thus making possible satellite and terrestrial communication links. Today, microwave communication systems handle a big frac-

tion of the world's telephone, data and television transmission. Modern wireless telecommunication systems such as direct broadcast television, cellular video systems, global positioning satellite systems operate in the frequency range 1.5 to 95 GHz, and therefore rely heavily on microwave technology.

1.4 Modulation Methods

In communication systems, information is transmitted using modulation techniques. Modulation is the process of encoding information from a message source in a manner suitable for transmission. Modulation is used to overcome the risk of overlapping or jamming that would occur if signals were transmitted at their natural bandwidths. It also helps to increase the speed of communication because some carrier wavelengths are more conveniently generated and propagated than wavelengths in the message. Modulation generally involves translating a baseband message signal to a band- pass signal centered at frequencies that are very high compared to the baseband frequency. The baseband signal is called the modulating signal and the band-pass signal is called the modulated (or carrier) signal. The modulation index therefore is defined to describe how much the modulated variable of the carrier signal varies around its un-modulated level. Today, modulation is done by many ways, both digital and analog. In this thesis, we discuss two most popular analog encoding methods: Amplitude modulation (AM) and Frequency modulation (FM). AM is seen to be the simplest technique to encode the information into the carrier signal. In AM, the amplitude of the modulated signal is varied in accordance with

the amplitude of the message signal. The information thus is stored in the amplitude of the carrier signal and is transmitted with the speed of the carrier frequency. The modulation index k of an AM signal is the ratio of the peak message signal amplitude to the peak carrier amplitude. The spectrum of the AM signal appears simply as symmetrical sidebands around the carrier frequency in which the spectrum width is double the bandwidth of message signals. The sidebands above and below the carrier frequency are called upper and lower sideband, respectively.

FM is a part of a more general class of modulation known as phase modulation. Phase modulation varies a carrier signal in such a way that the angle of the carrier is varied according to the amplitude of the modulating baseband signal. In FM, the amplitude of the carrier signal is kept constant while its instantaneous frequency is varied linearly with the modulating message signal. Thus FM signals have all their information in the phase or frequencies of the carrier. The FM modulation index β defines the relationship between the message amplitude and the bandwidth of the carrier signal. The spectrum of an FM signal usually is a complicated function and depends strongly on the message signal.

Fig. 1.1 illustrates AM and FM methods with a sinusoidal modulating signal x(t) both at the fifty percent modulation index. The AM signal spectrum consists of a sharp component at the carrier frequency and two sidebands which replicate the message spectrum while the spectrum of the FM signal consists of a carrier component and an infinite number of sidebands located on either side of the carrier frequency, spaced at integer multiples of the modulating frequency. The amplitude of the spectral components are given by the Bessel function of the modulation index

β.

In communication applications, FM provides many advantages over AM. Since message signals are represented as frequency rather than amplitude variations, FM signals are less susceptible to noise which tends to cause rapid fluctuations in the amplitudes of the received signals. It is possible in FM systems to trade off bandwidth occupancy for improved noise performance due to a variable modulation index. It can be shown that, under certain conditions, the FM signal-to-noise ratio improves by 6dB for each doubling of bandwidth occupancy [51]. Moreover, an FM signal is a constant envelope signal hence the transmitted power of an FM system is constant regardless of the amplitude of the message signal. In AM, however, it is critical to maintain the linear relationship between the applied message and the amplitude of the transmitted signal, thus, only linear amplifiers- which are not power efficient- are used in AM system. FM also exhibits a capture effect characteristic that is a direct result of the rapid nonlinear improvement in received quality for an increase in received power [51]. This inherent ability to pick up the strongest signal and reject the rest make FM systems very resistant to co-channel interference and provide excellent received quality. In AM, all of the interferences are received at once and must be discriminated. Combining the benefits that FM brings to communication, with the deterministic properties of chaos, an FM chaotic microwave signal is an ideal candidate for communication applications. This thesis presents both numerical modeling and experimental realization of a system that uses time delay and nonlinearity to generate FM chaotic microwave signals.

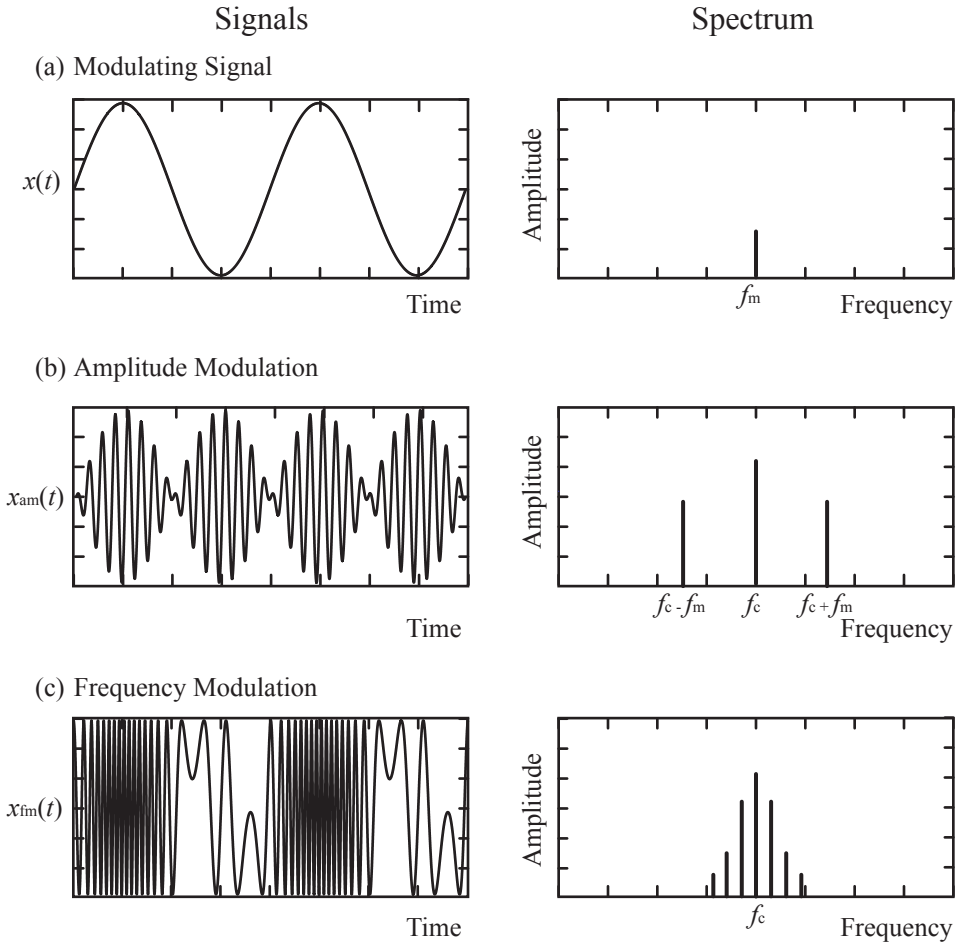

Figure 1.1: The demonstration of amplitude modulation (AM) and frequency modulation (FM) with the message as a simple sinusoidal signal with frequency f_m. The information is stored in the amplitude of the carrier signal in AM and in the frequency of the carrier signal in FM. The spectrum of AM signals consists of an impulse at carrier frequency f_c and two side bands at $f_c + f_m$ and $f_c - f_m$. The FM signal has a spectrum of a carrier frequency f_c at the center and two symmetric infinite side bands.

1.5 Deterministic Brownian Motion

Brownian motion is named in honor of the Scottish naturalist and cleric Robert Brown (1773-1858), who, while looking through a microscope at grains of pollen suspended in water, noticed that a group of grains always disperses and that individual grains move around continuously and irregularly. Upon systematically observing these irregular motions in pollen from live and dead plants, in pieces of other parts of plants, in pieces of animal tissue, in fossilized wood, in ground window glass, volcanic ash, siliceous crystal and even in a fragment of the Sphinx, Brown reasoned that the movement must be due to physical causes, rather than an irreducible elements to a vitality common of all life forms. In 1905, Brownian motion was explained by A. Einstein as a consequence of the atomic theory of matter [52]. When a particle is suspended in any fluid or air, the atoms or molecules composing the fluid/ air hit the particle from different directions in unequal numbers during any given time interval. While we cannot see the effect of individual molecular impacts, the net motion caused by many impacts over a period of time can be observed. Brownian motion is therefore a macroscopic manifestation of the molecular motion of the liquid. The mathematical foundation for Brownian motion was established 13 years later by N. Wiener when he presented the motion as a random process in a series of papers [53]. From there, physicists and mathematicians have developed and analyzed different statistical processes to create an accurate description of the Brownian motion. In the context of this thesis, we discuss three basic properties of the Brownian motion to distinguish it from other random dynamical behaviors. They

are: Gaussian distribution of the displacement of Brownian particles over a given time interval, self similarity, and continuous path. Consider a Brownian motion in a plane with x and y coordinates. If one records the positions of the Brownian motion at discrete time intervals, then the jumps in both x and y directions and the jump length (as a normalized step length between recorded points) follow Gaussian probability distributions. The self-similarity or martingale property of a Brownian motion is evident when one zooms into the trajectory and finds the similar irregular motion no matter what how much the magnification is. The paths of Brownian motion are continuous as the motion is a continuous stochastic process even though they are not differentiable. With these properties, one can easily construct a Brownian motion using numerical methods to randomly select steps from a Gaussian distribution with a small enough time increment. An n-dimensional Brownian motion is simply an n-dimensional vector of n independent Brownian motions. Today, Brownian motion is widely used in physics and finance for modeling random behaviors that evolve over time such as diffusion processes, the prices in the stock market, or the effect of price stabilization scheme in investment when demand is uncertain. It also forms the basis for the development of an enormous branch of mathematics centered on the theory of Wiener processes [54].

Brownian motion in fact is a special member of a larger family known as fractional Brownian motion, a generalization of Brownian motion suggested by Kolmogorov in 1940. The index used to differentiate members in this family is the Hurst exponent H which quantifies the relative tendency of a time trace either to regress strongly to the mean or to cluster in a direction [25, 28]. The value range

of H is $0 \leq H \leq 1$ where the special case when $H = 0.5$ gives regular Brownian motion. Traces corresponding to values of H smaller than 0.5 have a tendency to turn back upon themselves: the property is known as anti-persistence. On the other hand, with the values of H larger than 0.5, the traces persist in its progression in the direction in which it was moving. For a dynamical system, the Hurst exponent can span the full range of values as a function of system parameters.

Deterministic Brownian motion is a Brownian motion produced by a deterministic process without introducing the assumption typically associated with the theory of random processes as for regular Brownian motion. There are numerous reports on the existence of Brownian-like motion from deterministic dynamics both in discrete maps and flows [55–62]. The first model of deterministic Brownian motion was proposed by C. Beck [55] in which the Brownian particle is subjected to a dissipative drag and impulsive kicks that occur at a time scale of the fluctuation. The amplitude of fluctuation force is derived from chaotic phase-mixing maps. Beck had shown that when the time scale approaches zero, the discretized dynamics of the Brownian particle converges to a Langevin equation describing an Ornstein- Uhlenbeck process which implies that the corresponding motion in the position space is diffusive with a Gaussian distribution. The work by Chew and Ting investigated a further limit of the model in momentum space when the fluctuation time scale is large [61]. They used the logistic map to derive the fluctuation force, and showed that the model can exhibit Gaussian diffusion process in position while the discretized momentum variable has a stationary, non- Gaussian distribution. Other chaos mappings have been applied to the model such as a booster process map [62]

to show that the erratic trajectories observed in Brownian motion could be explained without introducing a statistical assumption or thermodynamic limit. The recent work by J. Lei and M. C. Mackey in [63] pointed out that deterministic Brownian motion could be generated from delay differential equations.Their numerical model was developed from the Beck model with the assumption that the fluctuation force could be continuous in time, and depend on the state of the particle with a lag time. The results show that the system's equation (which is delay differential equation in a suitable parameter region) can generate dynamics with many of the properties of the Brownian particle in spite of the fact that the evolution equation is genuinely deterministic. The second theoretical model of deterministic Brownian motion is developed from a Hamiltonian formalism in which the dynamics of Brownian motion is viewed as a system of heavy particles interacting with a bath of light molecules [59, 60]. Because the particle is heavier than the molecules, one can view the particle as a slow dynamical system relative to the molecules. Using the projection operator after integrating the fast variables out, Brownian motion can be modeled by a Langevin equation which embodies the macroscopic physics of Brownian motion. This approach treats the fluctuation forces as a Gaussian distributed stochastic process while leaves open questions about intrinsic Brownian motion. The model thus is used widely by mathematicians to explain stochastic processes. Experimental evidences of deterministic Brownian motions were also reported by the observation of long time trajectories of a colloidal particle undergoing Brownian motion in liquid [58].

In this thesis, we illustrate the existence of deterministic Brownian motion

numerically and experimentally from a simple time delay differential equation that describes our microwave circuit. We discuss further the possibility of synchronization of two systems exhibiting deterministic Brownian motion and stability of the synchronization.

1.6 Outline of Thesis

In this introductory chapter, we have provided the motivation for studying the subject presented in the thesis. The following chapters will be devoted to experimental set up, numerical models, dynamics and applications of microwave time-delayed feedback loops.

In chapter 2, we introduce the components of an isolated microwave time-delayed feedback loop, which includes a voltage controlled oscillator, a mixer, transmission lines, digital voltage integral and time delay functions. For each loop component, we briefly discuss the circuit and electronic implementation and develop a mathematical model. We also present the experimental measurements that verify the device characteristics.

In chapter 3, we analyze the signal path to develop the system equations. We study the equations to find the bifurcation points. The way of generating a set of initial conditions along with numerical methods are described. We also discuss the measurement of chaos by presenting the Lyapunov exponents and Kaplan- Yorke dimension which can be computed from the model.

Chapter 4 is devoted to the study of dynamical behaviors of a microwave

time-delayed feedback loop for two different nonlinear functions: sinusoidal and Boolean. The numerical results and experimental observations of time series are presented. We also construct the bifurcation diagrams as system parameters are varied smoothly. The frequency spectrum, Lyapunov exponent and Kaplan-Yorke dimension are shown for the case of chaotic microwave frequency modulated signals.

In chapter 5, we study the microwave time-delayed feedback loop in a higher gain regime where deterministic Brownian motion is possible. The experimental results and numerical simulations are illustrated along with the Gaussian process. We calculate the Hurst exponents of the Brownian traces for different values of the system parameters to show the existence of fractal Brownian motion. We conclude the chapter by presenting the theory of synchronization between two feedback loops exhibiting deterministic Brownian motion.

Chapter 6 provide the summary of the thesis. We explain the significance of the results by showing an application of the chaotic FM signal in radar systems. Future directions in terms of experiments and analyses are also discussed.

Chapter 2: Components of a Microwave Time-delayed Feedback Loop

Over the past thirty years, scientists have proposed and demonstrated many effective methods to produce chaotic signals. A popular method dates back from early 1980 when Ikeda [64] introduced a way to generate chaos using basic electronics devices comprising a delay feedback loop. The novelty of this architecture has been proven by a wide collection of chaotic systems ranging from optics to electronic to microwaves [43, 65, 66]. In this chapter, we describe the design of a microwave chaotic signal generator that employs commercial microwave components together with time-delayed feedback through a field-programmable gate array (FPGA) signal processing board. We first present an overview of the loop, followed by basic electrical properties of key components such as the voltage controlled oscillator, RF mixer, transmission lines, a digital implementation of voltage integration and time delay.

2.1 Description of a Microwave Time-delayed Feedback Loop

The time-delayed feedback loop considered here is composed of a nonlinear element, amplifier, time-delay, and band-limiting filter. The nonlinear element is necessary for a system to exhibit aperiodic behavior. Several types of nonlinear functions

have been employed in feedback loops to produce chaotic dynamics. Interferometry optical systems (such as a Mach-Zehnder intensity modulator) produce a cosine-squared nonlinearity [43]. Some electronic systems use transistor circuits [65]for nonlinearity, however, this nonlinear function is hard to describe mathematically, and depends sensitively on the transistor bias. The delay can be produced by signal propagation through a span of optical fibers or transmission lines. It also could be implemented using a series of LC delay units. The filter functions are generated using commercial electronic devices such as op-amp, resistors and capacitors. With the availability of low-cost digital signal processing hardware, the electrical filtering and signal delay can also be conveniently implemented digitally, which has the advantage of allowing flexible adjustment of parameters.

An experimental illustration of a microwave time-delayed feedback loop is shown in Fig. 2.1 in which the nonlinear element consists of analog microwave devices while the rest of the loop is digitally implemented via discrete-time signal processing using a field programmable gate array (FPGA) board. The path of a signal in the loop is described as following: A microwave- controlled oscillator (VCO) provides a constant- amplitude microwave signal with an output frequency that is a linear function of the applied tuning voltage. The microwave signal then splits into two paths, one of which is phase-delayed with respect to the other by an amount of delay of several the microwave signal cycles. The amount delay is controlled by the length of a semi-rigid microwave cable, which is designed to have a group delay of 5ns/m. The two signals are fed into a double-balanced mixer, completing a homodyne phase discriminator as depicted in the figure. This phase discriminator is assembled on

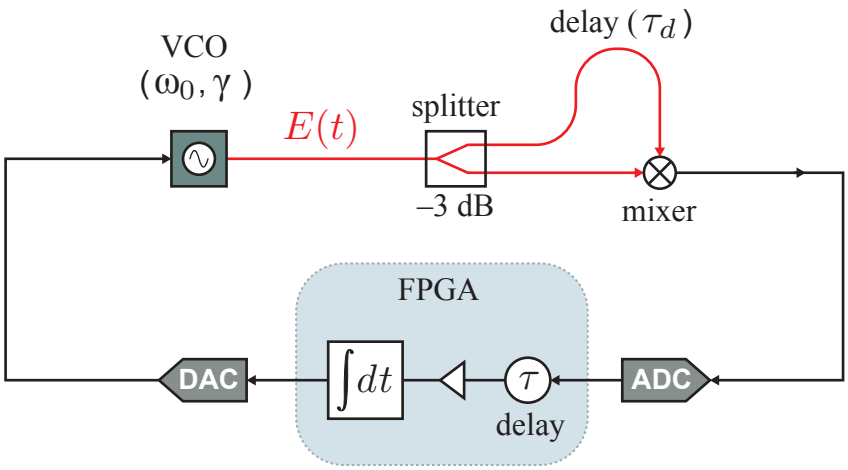

Figure 2.1: Experimental microwave time-delayed feedback system. The system uses a conventional microwave voltage-controlled oscillator (VCO) with a homodyne microwave phase discriminator to produce a sinusoidal nonlinearity. The output is then fed back to the input through a time-delayed integrator.

a microwave printed circuit board and, together with the VCO and delay line, can produce an output signal that is a sinusoidal function of the voltage applied to the VCO, thus producing the nonlinearity in the loop. The output of the mixer is then fed back to the VCO input voltage through a time delay and a filter. The amount delay (which from now, is denoted by the signal delay to differentiate from a short time delay used in microwave band) as well as the gain of the integrator could be changed smoothly by programming the logic circuits inside of a FPGA board. To understand dynamical characteristics of the loop, we investigate in detail electric properties of each component, starting with voltage controlled oscillator.

2.2 Voltage Controlled Oscillator

Voltage controlled oscillator (VCO) is one of the frequently used microwave sources used widely in microwave engineering, especially in modern microwave communication systems. A VCO is a device that converts an input baseband analog voltage into a signal whose frequency is a proportional linear function of the applied input voltage. There are two popular types of analog VCOs, characterizing by the waveforms they produce: relaxation VCO which can generate saw-tooth or triangular signal and harmonic VCO that can emit the sinusoidal waveform. In the microwave time-delayed feedback loop that is the subject of this thesis, we use the harmonic VCO because of its advantages of frequency stability with respect to temperature, noise and power supply's fluctuations. A harmonic-type VCO circuit consists of an amplifier that provides adequate gain and a resonant circuit that feed

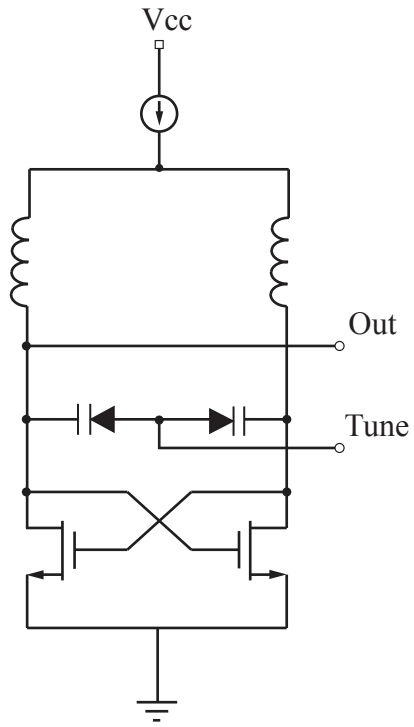

Figure 2.2: A typical monolithic circuit implementation of the VCO used in our system. This process technique allows VCOs to have a compact size, easily integrated with other microwave devices

the signals back to the input. Oscillation occurs at the resonant frequency where a positive gain arises around the loop. Fig. 2.2 shows a typical monolithic VCO circuit implementation used in our system.

The input voltage of a VCO is called *tuning voltage* or *tuning signal*. The tuning voltage amplitudes of most VCOs can go from 0 to 5 V with the *tuning bandwidth* varies up to few MHz. The *tuning bandwidth* or *modulation bandwidth* of a VCO is the range of tuning signal's frequencies where the VCO performs normally without losing too much power. The *tuning sensitivity*, which we denote γ, is given in units of Hz/V and describes the proportionality factor between the voltage and

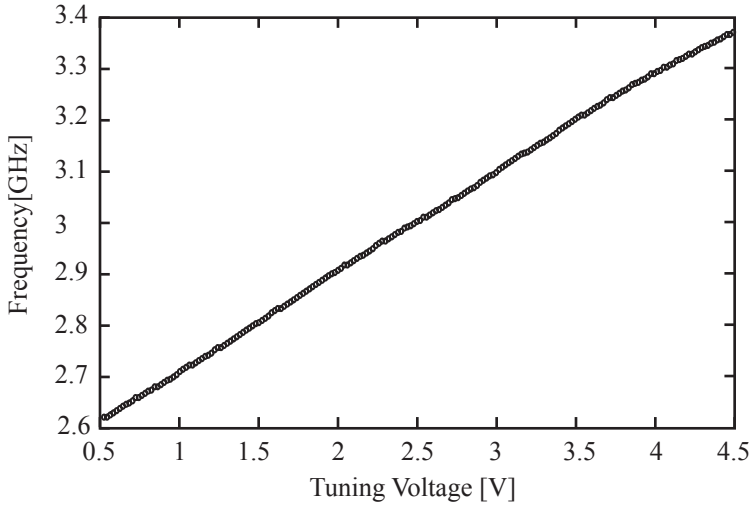

Figure 2.3: The tuning curve of the VCO used in our system. The base frequency as y-intercept, $f_0 = 2.6$ GHz; tuning sensitivity as the slope is measured using a linear interpolation, $\gamma = 180$ MHz/V

RF frequency. The frequency of the oscillator when no input signal is applied is called the base or natural frequency, denoted f_0. Another important characteristic of VCO is its phase noise which describes short term random frequency fluctuations or the degree to which a VCO maintains the same value of frequency over a given time. The phase noise of the VCO is therefore determined primarily by the overall quality factor Q of the circuit. In order to design a circuit with high Q, the tuning bandwidth must be made small. Therefore, a VCO designed for low phase noise performance will have a smaller tuning range.

Fig. 2.3 displays the experimentally measured tuning curve of the microwave VCO (Mini-Circuits SOS-3065-119+) [67] used in our system. The frequencies of the microwave output signals were measured using spectrum analyzer while the

tuning voltages were varied smoothly. The tuning range is from 0.5 to 4.5 V and has an electrical input bandwidth of 10 MHz. The typical phase noise of the VCO is -56 dBc/Hz at offset frequency of 1kHz. The base frequency, f_0, is 2.6 GHz; and the tuning gain γ is estimated to be 180 MHz/V. The VCO can therefore sweep its frequency over a 700 MHz range within the C-band of the electromagnetic spectrum. This frequency band matches the frequency range of the microwave communication networks such as those used for cell-phones, radar, satellite communication and WiFi. The nonlinear part of the tuning curve is due to non-ideal properties of reactor diodes at the edge of tuning range such as the microwave output signal has non-constant amplitude due to the effect of varying frequency.

The microwave signal produced by the VCO is sent to a 3 dB splitter which is a linear device to split into two identical microwave signals, each with half power. One of these signals is then delayed by an amount of 10 ns by a 2 m length semirigid microwave cable. The two signals are finally fed into a double-balanced mixer. The mixer is a nonlinear device whose characteristics will be discussed in the next section.

2.3 Microwave Mixer

Microwave mixers translate the frequency of electromagnetic signals. This functionality is vital for an enormous number of applications ranging from military radars and surveillance to radio astronomy to biological sensing networks [68]. Microwave mixers are nonlinear electrical devices that are designed to mix (or multiply) two microwave input signals, and producing a low frequency baseband electri-

cal signal at the output. (They are also used in reverse, to up- convert a baseband signal onto a microwave carrier). Despite their ubiquity, however, microwave frequency mixers remain one of the most misunderstood components available in the RF/microwave engineer because of its nonlinear properties.

A frequency mixer is a 3-port electronic circuit. Two of the ports are input ports and the other is an output port. The ideal mixer multiplies the two input signals such that, after filtering, the output signal frequency is either the sum (up-conversion) or difference (down-conversion) frequency of the inputs. The terms for the 3 mixer ports are the Local Oscillator (LO) port, the Radio Frequency (RF) port, and the Intermediate Frequency (IF) port. The LO port is typically driven with either a sinusoidal continuous wave (CW) signal or a square wave signal. The choice to apply a CW or square wave signal depends on the application and the mixer. The IF/RF signals tend to be information-bearing signals. During frequency conversion, the information carried by the RF/IF signal is frequency translated to the IF/RF output. Therefore, mixers perform the critical function of translating in the frequency domain.

The most important figure of merit of a mixer is conversion loss which is a measure of the efficiency in providing frequency translation from the RF/IF input signal to the IF/RF output signal. Conversion loss is defined as the ratio in power between the input RF power level and the desired output IF frequency power level [48]:

$$L_c = 10log\frac{\text{available RF input power}}{\text{IF output power}}\,(dB)\,. \tag{2.1}$$

Typical values of conversion loss range between about 4.5 to 9 dB, depending on the mixer. For a down-converting mixer, since the output frequency has been shifted down or reduced, the conversion loss becomes the down conversion gain which tells us how much the IF was attenuated. Other mixer terms which relates closely to conversion loss are isolation and compression. Isolation is a measure of circuit balance within the mixer or the amount of power that leaks from one mixer port to another [69]. Three types of isolation are commonly quoted in microwave mixers: L-R isolation, L-I isolation and R-I isolation. Since the RF power is normally smaller than the power drive at LO, the R-I isolation is not an important factor to evaluate mixer. The L-R (L-I) isolation is the amount of the LO drive power get attenuated when it is measured at the RF (IF) port while the IF(RF) port is terminated by a 50 Ω load. The higher the LO isolation means smaller power leak through the ports. The compression point of a mixer (normally named 1dB compression) is a measure of the linearity of the mixer and is defined as the input RF power required for which the mixer will provide the linear operation in terms of conversion loss. Conceptually, the 1 dB compression point occurs when the RF signal can no longer be considered a small signal, normally when the RF power is within 10dB of the LO drive level. Mixer compression usually changes with the LO power level. It is therefore important to select a mixer which has input drive level that affords the required compression point for the application [70].

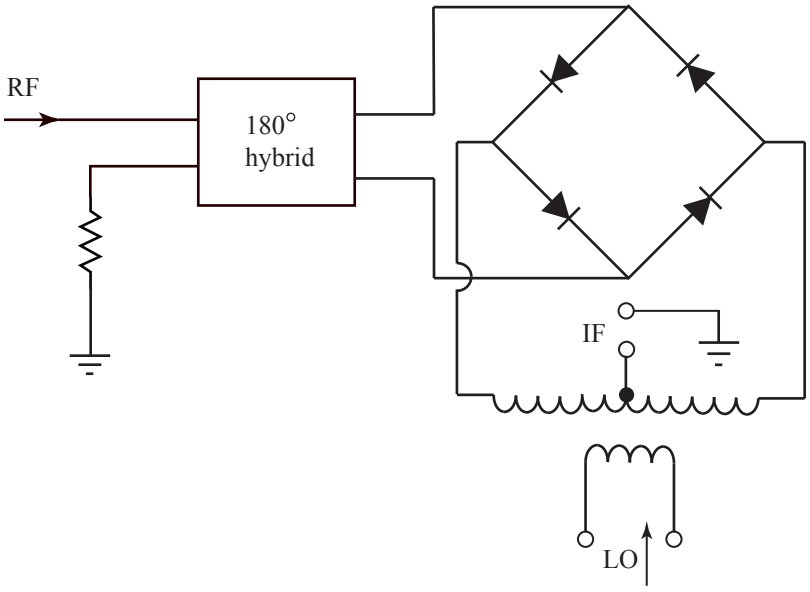

Figure 2.4: The double balanced mixer is composed of a diode ring and the 180° hybrid junctions. The design helps the mixer to have better isolation and higher conversion gain.

The mixer used in our system is a double-balanced mixer whose schematic diagram is illustrated in Fig. 2.4. The mixer circuit which consists of four diodes configured in a ring and two 180° hybrid junctions. The circuit symmetry helps to have a better isolation among all mixer ports, especially the RF/LO isolation. It also can give cancellation of AM noise from the LO port. Both are resulting in a lower conversion loss. The hybrid junction, which is a four port circuit that provides mutual isolation between input ports and equal power division at the output ports, helps to isolate the input LO and RF from one another, thus providing frequency band independence and equal power division to the load [69].

The double-balanced mixer used in our system (Mini-Circuits MCA1-80LH+) [71] has typical RF/LO isolation of 35 dB and a down conversion gain of 6 dB. The mixer output frequency ranges from DC to 1250 MHz while LO and RF frequencies ranges cover the whole C and S microwave bands. This low noise and high efficiency double-balanced mixer meets the designing requirements of a mixing component in our feedback loop.

Since all the components of the homodyne phase discriminator operate in microwave frequencies, the connections between them are transmission lines. This is due to the fact that the physical dimensions of microwave devices are a considerable fraction of a wave length or many wavelengths. The circuit theory and normal electrical wires thus cannot be used. Also, impedance mismatch in microwave systems can cause significant power loss. Therefore, designing and implementing appropriate transmission lines are critical for our microwave feedback loop. We will discuss this process in next section.

2.4 Microwave Transmission Lines

The term transmission line is commonly reserved in electromagnetic for those structures which are capable of guiding Transverse Electromagnetic (TEM) waves. As a special class of the more general electromagnetic wave guides, transmission lines, help to transmit electrical signals between two points in space. There are different types of transmission lines used in various range of frequencies such as wires, coaxial cables, electric power lines. Another way to classify transmission lines is by the number of orthogonal physical dimensions. For example, a coaxial line might be considered one dimension (its length), a transition from a coaxial line to a strip line would be considered three dimensional, and a lumped element has zero dimensions. One can always model the transmission line by a lumped-element circuit made up of RLC network [48, 68] . With the aid of Maxwell's equations and Kirchhoff's laws, the characteristic impedance of an ideal transmission line could be derived. This value is independent of frequencies which provides the perfect method for power transfer in high frequency systems. However, a transmission line is usually not an isolated component but is terminated by load impedances in the circuit. As a result, the wave on the transmission line now is a superposition of an incident and reflected (standing) wave. To minimize this reflection effect, one must use load impedance that is matched to the characteristic impedance of the transmission line.

With their physical dimensions as the criteria, one can categorize microwave transmission lines as three groups: coaxial lines, rectangle and circular wave guides, and strip-type transmission lines. The most popular microwave transmission lines

used are coaxial lines. They are very convenient for test application with the operation frequencies can go up to 5 GHz. Because of the large physical size, they are a difficult medium to fabricate with complex microwave components. Rectangle and circular wave guides are one of the earliest types of microwave transmission lines. They are cheap to build and have high power capacity which is very useful in many precision test applications. The wave guides operation bandwidth however isn't as high as in coaxial lines. Strip-type transmission lines stand out with advantages such as compactness, low cost and easy integration with active devices to form microwave integrated circuits. Their small physical dimension fits in with the recent trend toward to the miniaturization and integration in microwave communication. There are two types of strip-type transmission lines which differ in their geometrical symmetry: symmetric strip transmission lines or strip lines, and asymmetric transmission lines or micro-strip lines, as illustrating in Fig. 2.5.

With the goal of constructing a compact stable system to generate microwave chaotic signals, we put the homodyne phase discriminator on a printed circuit board with a continuous ground plane. The micro-strip lines therefore the best-suited transmission line for this application. We start to design these connections by first specifying the dielectric material and then calculate the required width of the top conductor as well as the required thickness of the board. Since our microwave phase discriminator functions in C-band of microwave bandwidth (frequencies from 2-4 GHz) and the goal is to generate chaotic microwave signals which are sensitive to any small change in initial conditions, we must choose a material with low loss at high frequencies and less dependent on any frequency fluctuation. Rogers 4350B

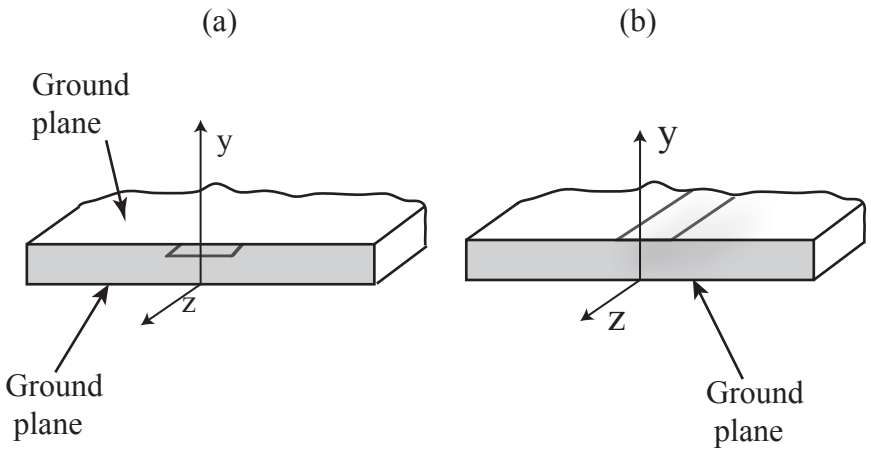

Figure 2.5: The geometry of a strip line (a) and a micro-strip line (b).

satisfies such requirements. The thickness of the printed circuit board is chosen as one of standard thicknesses recommended by the manufacturer. In our case, it is 0.508mm. Since all of the microwave devices used in the loop have 50 Ω impedance, we calculate the width of micro-strip lines equal to 1.12 mm to yield the same value using impedance formulas in [72]. The design is then simulated using high frequency structural simulator (HFSS) to verify the impedance and S parameters. The physical dimension of the micro-strip line is reasonable to fabricate.

Fig. 2.6 (b) shows our finished microwave printed circuit board with Ro4350B as a dielectric material, copper as a metal; the bottom layer of the board is grounded continuously. The board is illustrated along with the block diagram in Fig. 2.6 (c).

To test the nonlinear function provided by the self-homodyne phase discriminator, we varied the tuning voltage of VCO from 0.5 V to 3.5 V and recorded

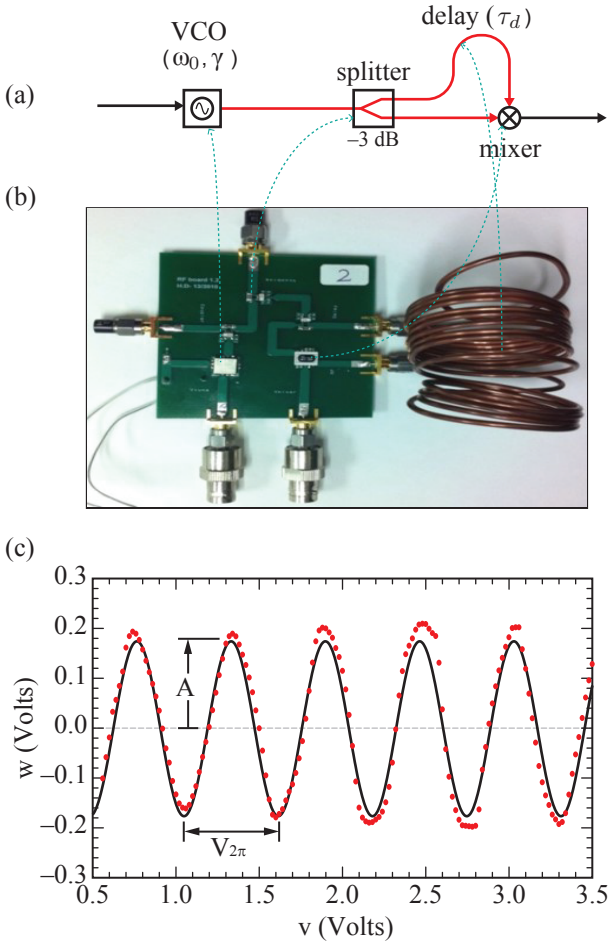

Figure 2.6: (a) The block diagram of the self- homodyne phase discriminator. (b) The implementation of the self-homodyne phase discriminator: a finished microwave printed circuit board, where all the components are put on a continuous ground plane. The transmission line is made by Rogers 4350B with 1.12 mm wide to yield 50 Ω impedance. (c). Experimental measured relationship between input $v(t)$ and output $w(t)$ of the self- homodyne phase discriminator comprising 10 ns microwave delay line and mixer. The solid curve is the best-fit sinusoidal function.

the value of mixer output using a multi-meter. Fig. 2.6 (c) plots the experimentally measured sinusoidal relationship between the tuning voltage v and the mixer output w, together with a best-fit sinusoid. From these measurements, one can determine the two constants $A = 0.2$ V and $V_{2\pi} = 0.5$ V. The deviation from a perfect sinusoidal nonlinearity is attributed to non-ideal voltage-dependent power from the VCO and non-ideal mixer characteristics. The output of the mixer is electronically integrated and time-delayed and then being fed back to the VCO. From here, the signal has the frequency as low as DC. We therefore design a delay and voltage integral functions with appropriate values to complete the feedback loop. The delay integrated feedback part of the loop is discussed in the next section.

2.5 Time Delay and Voltage Integral Functions

In this section, we will discuss the time-delayed and voltage integral functions which are the components that operate in baseband frequencies in our feedback loop. The voltage integrator has a low-pass bandwidth due to the finite gain at DC. Since the mixer output has frequency range from DC to 1250 MHz but tuning bandwidth of the VCO is in the order of 10 MHz, the voltage integrator sets the upper frequency limit of the signal coming out from the mixer to fit within the tuning bandwidth. The time-delayed function is scaled to the integrator bandwidth so that the feedback loop functions in band-pass frequencies of microwave discriminator.

In our system, the time-delayed integrated feedback part was constructed digitally using a field-programmable gate array (FPGA) board. A FPGA is an in-

tegrated circuit designed to be configured by a customer or a designer after manufacturing. Unlike other digital processing boards, the configuration of a FPGA is specified using a hardware description language on a series of logic gates. The FPGA used in our system (Altera Cyclone II EP2C5) has a high-density architecture with 4608 logic elements (LEs) and twenty-six M4K embedded memory blocks along with 1.1 Mbits of RAM available without reducing available logic. The circuit allows the flexible clock management with programmable duty cycle, external clock outputs and two phase-locked loops (PLLs) available for clock multiplication and division. It also provides up to 622 usable Input/output pins and thirteen embedded multipliers. The FPGA therefore can support a high level, complex design at low cost and low power consumption. To combine the FPGA with our analog microwave components, we use a FPGA board (Saxo Q) whose the general block diagram is shown in Fig. 2.7. The board uses a USB interface to power and configure FPGA. In addition to the embedded memory, this board offers 4 Mbits for FPGA boot-PROM to conveniently store programs. The two 8-bit 200 MSPS analog to digital converters (National Semiconductor, ADC 08200) [73] and four 10-bit digital to analog converters (TI DAC 900) [74] connect the digital FPGA chip with the rest of the feedback loop. More detail about this FPGA board could be found at [75].

Implementing the delay and voltage integral functions on the FPGA board provides us the flexibility of varying the amount of delay and integral function's gain. This offers significant advantages over conventional analog filters and delay circuit when studying the dynamics of the loop because one can look at the system's dynamical behavior in wider range values of parameters. Furthermore, a FPGA

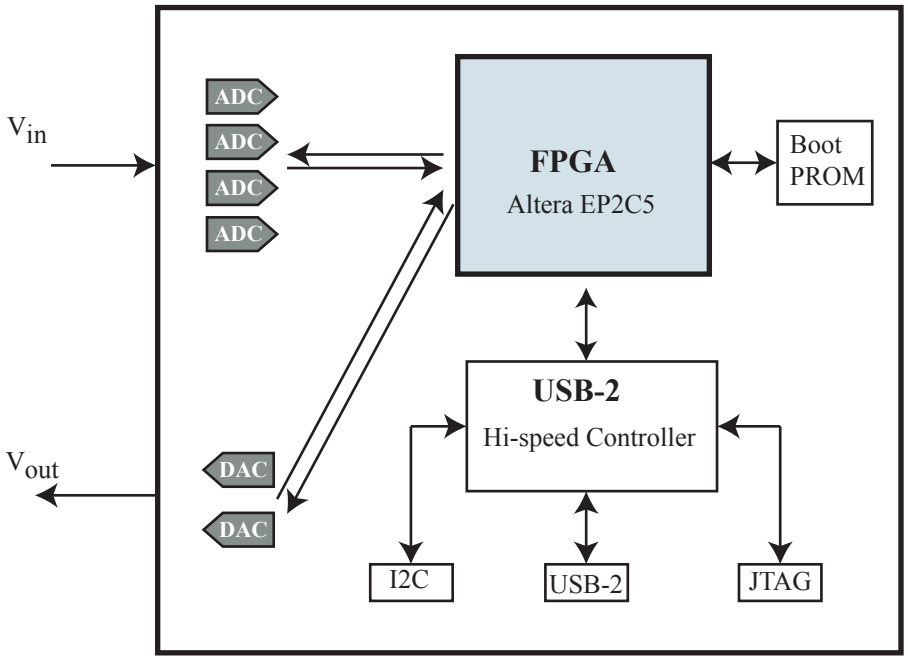

Figure 2.7: Simplified block diagram of a FPGA board. The board is powered and configured by a USB controller. The FPGA contains an analog to digital converter (ADC) that samples an incoming analog signal at regular intervals. The sampled data is then processed by programmed logic circuits on FPGA. The processed digital signal is then converted back into an analog signal by a digital to analog converter (DAC).

board is compact and easily to connect to other components in the loop unlike the normal analog implementation of voltage integrator and delay (using amplifier and basic elements such as inductors, capacitors and resistors). Incorporating the FPGA board in the feedback loop also has the advantage of allowing two separately constructed systems to be closely matched in their performance, which is essential to the study of synchronization dynamics.

The voltage integral function could be described by the mathematical relationship:

$$v_{out}(t) = \frac{1}{T} \int_{-\infty}^{t} v_{in}(t')dt'. \tag{2.2}$$

where T is the integration time constant. The continuous transfer function is written as following:

$$\hat{H}(s) = \frac{1}{Ts}. \tag{2.3}$$

Using bilinear transformation [76], when one can transfer the continuous variable s into a discrete one z:

$$s = \frac{2}{T_{sample}} \frac{z-1}{z+1}. \tag{2.4}$$

The transfer function could be written in discrete form as following:

$$\hat{H}z = \frac{T_{sample}}{T} \left(\frac{z^{-1}}{1-z^{-1}} \right), \tag{2.5}$$

The inverse z-transform gives the time-domain equation:

$$v_{out}[n] = v_{out}[n] + \frac{T_{sample}}{T} v_{in}[n-1], \tag{2.6}$$

which is seen to be a simple algebraic accumulator. The process of implementing a digital voltage integral function on FPGA is described as follows: The output

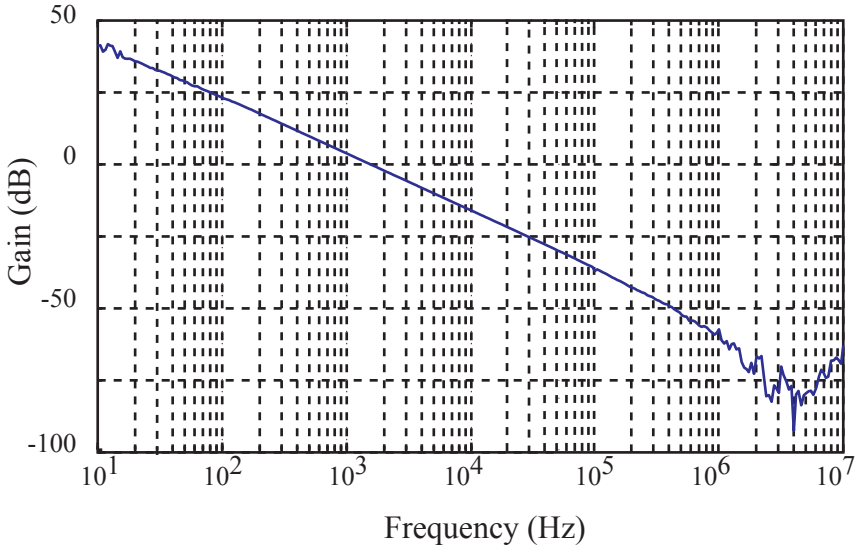

Figure 2.8: Measured amplitude response of a digital voltage integral function implemented on FPGA board. The noise at the low frequency is due to instrument artifact of the network analyzer.

analog signal coming from the mixer is sent to one of four analog inputs of FPGA board. It is then being sampled at regular time intervals using one channel of the ADC. The sampling interval, i.e. the time between samples, is set by configuring the sampling rate F_s. In our experiment, we use the frequency 75.7575 MHz generated by a local crystal oscillator on the board as the base clock for the ADC sampling frequencies. This odd frequency is guaranteed to be asynchronous to any periodic signals might occur on the FPGA (a condition required in equivalent time sampling mode). The digitized input sequences created by the ADC are manipulated by a programmable logic circuit to perform the simple summing accumulator in (2.6) on FPGA processor. The signal is finally converted back into an analog form using one of two DACs before being output.

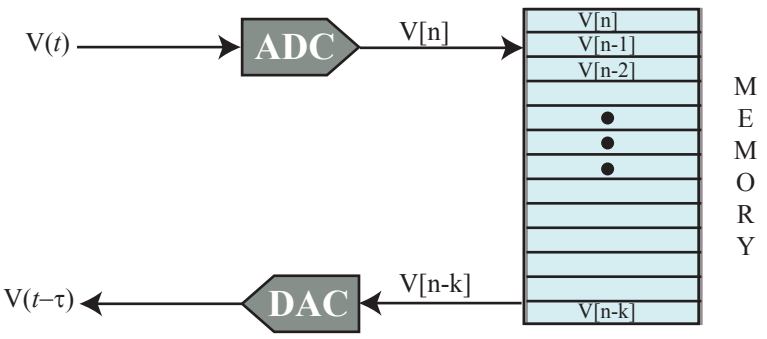

Figure 2.9: Digital time delays implement process on the FPGA. The digitized input signals are stored in a memory buffer before output by DAC.

Fig. 2.8 describes the measured amplitude response of the voltage integral implemented on FPGA at the sample rate of 15.15 Msample per second (which is derived using a PLL to perform frequency division on the basic 75.7575 MHz clock). The 3 dB bandwidth of the integrator is 1 MHz due to the finite gain at DC frequency. The noise observed at low frequencies is an instrument artifact that arises because the network analyzer used to measure the behavior cannot measure at low frequencies. The time constant T (as the slope of the frequency response curve) could be varied by changing the reprogramming FPGA.

The time delay function is created on the FPGA board using the shift register method which is illustrated by a block diagram in Fig. 2.9. The discrete-time samples from the ADC are collected in an indexed memory buffer of length k. At each sampling instant, the stored samples are moved down the buffer by one unit and

simultaneously the value in the k^{th} unit is output through the DAC. This process produces a time-delay equal to k sampling intervals. Thus by configuring the length of the memory buffer a desired delay can be set. With the flexibility to produce customized sample rates using two PLLs, and a large memory storage on FPGA, this method could create a large value of delay time up to minutes as well as vary this delay in a wide range. The delay time created by this method also is independent on frequencies. This is another advantage of the digital delay line over conventional analog electrical time delays implemented with either coaxial cables or a series of LC delay units. Moreover, the analog LC delay lines generally introduce additional frequency dependence that is undesirable. And implementation of a cable time-delay of the order of a few milliseconds requires an impractically long cable and can be very lossy. For the experiments reported here, we use the sample rate of 15.1515 Msample per second and a 600-stage shift register to create 40μs delay.

Chapter 3: Mathematical Model

In this chapter, we develop a mathematical model for the microwave time-delayed feedback loop. Because the system is connected in a feedback loop, it is possible to describe the dynamics in terms of the dynamical variable at any point in the loop. For convenience, we choose the VCO input as the point of reference, and derive a differential equation to describe the tuning voltage. The equations are derived by combining the mathematical description of the individual components of the feedback loop that were discussed in chapter 2. The present mathematical model, however, does not include electronic noise terms and assumes that all the components work ideally. Despite these simplifying assumptions, the model includes all the essential features of the dynamics by incorporating the nonlinearity, time delay and voltage integral functions.

We first analyze the signal path in the feedback loop to derive the mathematical description for the tuning voltage of the VCO. The equation is one of the simplest nonlinear delay differential equations [77] that exhibits chaotic behavior. In order to more accurately model the hybrid analog-digital experimental system, we re-write the differential equations in discrete-time as a recursive map equation. The method to solve for solutions is then presented, beginning with the analytical technique

to find the first critical value of the dimensionless system parameter at which the system undergoes a change in dynamical behavior (the first bifurcation point). The numerical method to compute the solutions is discussed along with the procedure for constructing a bifurcation diagram as the loop gain is varied. The chapter concludes with a discussion of dynamical metrics, namely the maximum Lyapunov exponents, spectrum of the Lyapunov exponents and Kaplan-Yorke dimensionality.

3.1 System Equation

As discussed in the previous chapter, the microwave signal generated by a VCO has a constant-amplitude with a frequency that varies linearly with an applied tuning voltage. This output signal from the VCO can be described by the complex microwave signal:

$$E(t) = \sqrt{2A}e^{j[\omega_0 t+\theta(t)]} \tag{3.1}$$

where A is a constant that is proportional to the microwave power, the factor of $\sqrt{2}$ is for introduced to simplify the subsequent algebra; ω_0 is the natural frequency of the VCO (i.e., the free-running frequency when no voltage is applied), and the phase $\theta(t)$ is related to the applied voltage $v(t)$ by:

$$\frac{d\theta}{dt} = 2\pi\gamma v(t) \tag{3.2}$$

The factor γ is tuning sensitivity of the VCO a property of the VCO that represents the gain of a frequency modulation process in the VCO.

The signal $E(t)$ is sent to the 3dB microwave power splitter to create two identical signals. One of them is then delayed by an amount of τ_d from another.

The signals are sent to the mixer as the LO input:

$$E_{LO}(t) = \sqrt{A}e^{j[\omega_0 t+\theta(t)]} \tag{3.3}$$

and RF input

$$E_{RF}(t) = \sqrt{A}e^{j[\omega_0(t-\tau_d)+\theta(t-\tau_d)]} \tag{3.4}$$

The output IF of the down-converting mixer is described as following:

$$\begin{aligned} w(t) &= \frac{1}{2}\,\mathrm{Re}\Big\{E_{LO}(t)E^*_{RF}\Big\} \\ &= A\cos\left[\theta(t)-\theta(t-\tau_d)-\omega_0\tau_d\right] \end{aligned} \tag{3.5}$$

If we further assume that $\theta(t)$ varies slowly on the timescale τ_d, so that

$$\theta(t)-\theta(t-\tau_d) \approx \tau_d\frac{d\theta}{dt} = \tau_d 2\pi\gamma v(t) \tag{3.6}$$

The mixer output, therefore, maybe approximated as:

$$w(t) = A\cos\big[2\pi\gamma\tau_d v(t)-\omega_0\tau_d\big]. \tag{3.7}$$

Finally, the output signal of the mixer is fed back to the VCO tuning input through a time delay τ and integrating function, so that $v(t)$ and $w(t)$ are related by

$$v(t) = \frac{1}{T}\int_{-\infty}^{t} w(t'-\tau)dt' \tag{3.8}$$

where T is the integration time constant and τ is the feedback time delay, which is assumed to be much larger than the microwave delay τ_d. Differentiating (3.8) and making use of (3.7), we obtain a first-order delay differential equation for the tuning voltage $v(t)$,

$$\frac{dv}{dt} = \frac{A}{T}\cos\big[2\pi\gamma\tau_d v(t-\tau)-\omega_0\tau_d\big] \tag{3.9}$$

where the scale factor A is now understood to include the microwave power, mixer efficiency, splitter loss, and any baseband electrical gain in the feedback path.

We next define a normalized dimensionless voltage $x(t)$ as

$$x(t) \equiv 2\pi\gamma\tau_d v(t) - \omega_0\tau_d - \frac{\pi}{2} \tag{3.10}$$

which leads to the delay differential equation

$$\frac{dx}{dt} = -2\pi\gamma A\frac{\tau_d}{T}\sin\big[x(t-\tau)\big] \tag{3.11}$$

Furthermore, by normalizing time in terms of the feedback delay τ, (3.11) simplifies to

$$\dot{x}(t) = -R\sin\big[x(t-1)\big] \tag{3.12}$$

where the single dimensionless constant R is defined as

$$R \equiv \frac{2\pi\gamma A\tau_d\tau}{T}. \tag{3.13}$$

R is the system parameter that characterizes the gain and the dynamical time scales of the loop. R could be varied by changing the length of microwave cable, or the ratio of the time delay or the integrator time constant.

(3.12) is a realistic physical model for the microwave time-delayed feedback loop dynamics. It could be illustrated by a mathematical block diagram depicted in Fig. 3.1 The model assumes that all the components of the loop are ideal, and the electrical noise is small. The system equation appears as a nonlinear delay differential equation with single effective control parameter R. This equation was considered by Schanz et al. [78], who observed that phase-locked loops with a feedback delay

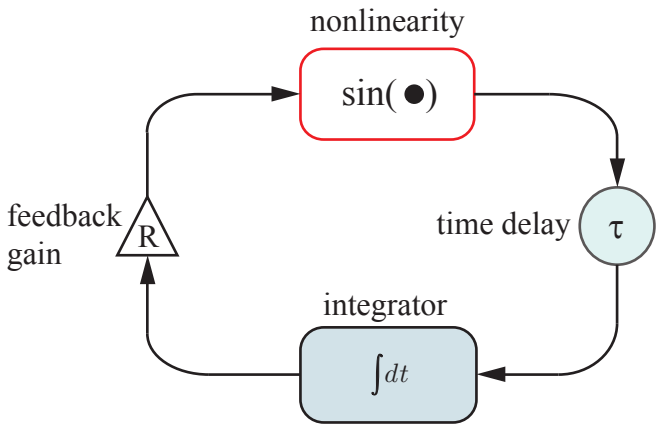

Figure 3.1: Mathematical block diagram of microwave time-delayed feedback loop.

can also be described by this equation. It was later independently analyzed by Sprott, who pointed out that it is one of the simplest nonlinear delay differential equations that can exhibit chaotic behavior [77].

When we use the FPGA in the loop to to implement delay and integration, the same mathematical model could be applied. However, because the FPGA uses discrete-time digital sampling, a mathematical description in discrete time is more appropriate. Instead of considering the variable $x(t)$ whose domain is all of time t, the discrete time solution is given only at the sample times nT_s where T_s is the time interval between successive samples of the ADC and n is an integer. The discrete feedback loop could be illustrated by Fig. 3.2, in which the integral and delay function are illustrated by digital implementation.

The digital delay and integral function are described in discrete time domain

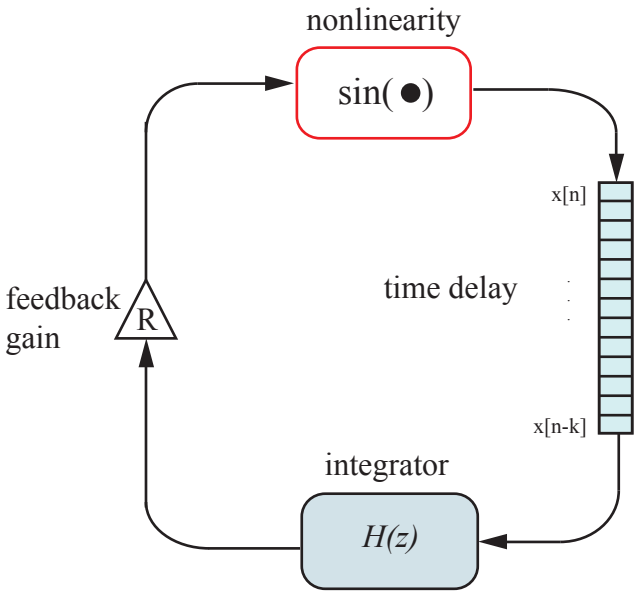

Figure 3.2: Mathematical block diagram of hybrid analog-digital microwave time-delayed feedback loop.$H(z)$ is taken the form of (2.5).

as a summing accumulator:

$$v(t) = v(t - \Delta t) + \alpha w(t - k\Delta t) \tag{3.14}$$

where Δt is the sampling period. The discrete-time parameters k and α determine the feedback delay τ and integration time constant T, respectively, according to:

$$\tau = k\Delta t, \qquad T = \Delta t \frac{1}{\alpha} \tag{3.15}$$

We next introduce the dimensionless system parameter G is defined as $G = 2\pi\gamma\tau_d\alpha$ such that the discrete-time system equation can be written as:

$$x\big[n\big] = x\big[n-1\big] + Gsin(x\big[n-N\big]) \tag{3.16}$$

This map equation is simple and captures all the features of the microwave time-delayed feedback loop. By iterating x while varying the parameter G, one can study how the dynamical behavior of the system depends on the gain. [79]. The method to numerically solve the system equation, both in continuous time and discrete time, will be discussed further in the next section.

3.2 Solution Methods

Like many DDEs, the system equation described here is impossible to solve exactly, because of the nonlinearity and the discontinuities that arise because of inconsistent initial conditions [80–82]. Consequently, solutions are approximated using numerical or analytical techniques and illustrated using the bifurcation theory. In this section, we present the method using both analytical and numerical techniques

to solve for bifurcation points (the points in which a small smooth change made to the parameter values of a system causes a sudden qualitative or topological change in dynamical behavior) of the system when the system parameter R is varied.

The common methods used to solve DDEs analytically are linear stability analysis [83], synergetic system analysis [84], and multiple scaling methods [78]. As one of the simplest DDEs, the some of the bifurcation points of the system equation of the microwave delay feedback loop can be solved exactly using these methods . We illustrate briefly here the process of finding the first critical value of R in which the system undergoes the sudden dynamical changes using the linear stability analysis method. As we recall the system equation (3.12)

$$\dot{x}(t) = -R\sin\big[x(t-1)\big] \tag{3.17}$$

The equation has the stationary solution $x_0 = l\pi$ in which l denotes an arbitrary number. To study the stability of these fixed points, we consider a small deviations x_{st} from x_0 as $x_{st} = x_0 + \epsilon(t)$ and insert this into the equation ((3.12)):

$$\dot{x}_{st}(t) = -R\sin\big[x_{st}(t-1)\big] \tag{3.18}$$

Linearizing the sin function near the stationary points gives us

$$\sin\big[x_{st}(t-1)\big] = \sin(x_0) + \cos(x_0)\epsilon(t-1) + \emptyset(\epsilon^2) \tag{3.19}$$

Dropping the higher order terms, we obtain

$$\sin\big[x_{st}(t-1)\big] \approx \cos(x_0)\epsilon(t-1) \tag{3.20}$$

The linearizion equation of the system around the stationary solutions $x_0 = l\pi$ is

written as

$$\dot{\epsilon}(t) = -R(-1)^l \epsilon(t-1) \tag{3.21}$$

Next, we establish the eigenvalue equation by inserting the general ansatz $\epsilon(t) = \Theta^\lambda e^{\lambda t}$ into (3.33) and considering the requirement for non-trivial eigenvectors:

$$\lambda + (-1)^l R e^{-\lambda} = 0 \tag{3.22}$$

For non-zero, positive values of R, the equation (3.22) admits solutions with real, positive values of λ if l is an odd integer number. The fixed point solutions $x_0 = \pi \pmod{2\pi}$ are therefore unstable. The stable fixed point solutions $x_0 = 0 \pmod{2\pi}$ will lose its stability when λ becomes pure imaginary, that is, when $\lambda = i\omega$. This condition leads to nonlinear algebraic system

$$R\cos(\omega) = 0 \tag{3.23}$$

$$\omega - R\sin(\omega) = 0 \tag{3.24}$$

The solution of the above system equation indicates that the first bifurcation point of the system occurs when the feedback gain $R_c = \pi/2$.

From (3.22), one can also calculate the first derivative of eigenvalues $\frac{d\lambda}{dR}$ as a function of feedback gain R as following:

$$\frac{d\lambda}{dR} = \frac{e^{-\lambda}}{Re^{-\lambda} - 1} \tag{3.25}$$

The condition $\left[d\lambda(R)/dR\right]|_{R=R_c}$ means that the Hopf bifurcation occurs at $R = R_c$ [26]. This result is confirmed with the multiple scaling method in [78] and the synergetic system analysis in [84] . The next system bifurcation points, however, are

hard to find analytically. Therefore, we use the numerical techniques implemented in Matlab to locate them.

The solution of an ODE is determined by its value at the initial point. For DDEs, we must provide not just the value of the solution at the initial point, but also the history the solution at times prior to the initial point. It has been proven that DDEs could be solved using an ODE solver that uses a modified way to generate initial conditions [80, 82]. The effective solvers for DDEs like *dde23* [80] involve the technique of breaking down the system history, thus, solving DDEs become a process of solving series of an initial value problem for an ODE in a time interval with a known initial point. Using this solver, one must keep track of how the discontinuity (generated from the breaking down history) at the initial point propagates due to the delay time. In our system, we use the method which utilize the same principle with *dde23* solver and iterate the system equation for long enough time for the transients to die down so that we could avoid the discontinuity. The system equation (3.12) can be understood in a compact way as:

$$\frac{dx}{dt} = \boldsymbol{f}(x(t-\tau)) \tag{3.26}$$

where $\boldsymbol{f}$ is a nonlinear function of the previous normalized tuning voltage. We can rewrite (3.26) from continuous evolution in delay time into iterative mapping at discrete but small time step $h = \tau/N$ where N is the number of steps

$$x(t+h) = x(t) + h\boldsymbol{f}(x(t-Nh)) \tag{3.27}$$

The above equations can be solved by any of the integration methods, such as Euler or Runge-Kutta in Matlab. Running the numerical calculation for different

parameter R values will give us a range of types of dynamics of the tuning signal separated by bifurcation points.

Generating the initial conditions of the system equation, however, is not an obvious step. The initial point and history of the equation should be produced randomly and have zero average. Because we do not know the dynamical state or the attractor, we begin the system from low amplitude noise. In practice, we run the simulation for long enough that the effect of our initial condition becomes irrelevant. We use the *randn* function in Matlab and averaging out the mean value to have a Gaussian distribution initial conditions around zero.

3.3 Measuring Chaos

Since chaos was discovered, scientists have developed different tools to differentiate chaos from noisy, random behaviors and and provide quantitative measures of the complexity of a chaotic system.. Some commonly used metrics for describing chaotic dynamics include the maximal Lyapunov exponent and Kaplan-Yorke dimensionality.

3.3.1 Maximal Lyapunov Exponent

The general acceptable definition of chaos states: chaos is an aperiodic, long term behavior of a bounded, deterministic system that exhibits sensitive dependence on initial conditions [28]. While it is straightforward to establish that a system is deterministic (i.e., there is no noise or random factors presenting in the system),

bounded and aperiodic, it is not clear how one could quantify the sensitivity of the system on initial conditions. In the context of this thesis, we use the Lyapunov exponent as the quantity whose sign indicates chaos and its value measures the rate at which initially nearby trajectories exponentially diverge. The Lyapunov exponent was named after the Russian mathematician Alexandr Lyapunov (1857-1918) who was the first to give out the complete definition of stability in order to quantify it in physical systems. General speaking, Lyapunov exponents measure the growth rates of generic perturbations, in a regime where their evolution is ruled by linear equations. In context of deterministic chaos, Lyapunov exponents quantify how fast the system diverges from one trajectory to another when initial conditions undergo a small change. For simplicity, we illustrate the concept of Lyapunov exponents in the context of iterated one-dimensional maps. This discussion is easily generalized to higher dimensional and continuous time systems.

Given some initial conditions x_0 of a one-dimensional map, consider a nearby point $x_0 + \delta x_0$, in which the initial separation δx_0 is an extremely small. Iterate the map n times and watch how the separation grows to δx_n. If one can describe the relationship of δx_0 and δx_n as $|\delta x_n| = |\delta x_0| e^{n\lambda}$, then λ is called the Lyapunov exponent.

For an n-dimensional map, there exists n Lyapunov exponents to characterize the growth of the separation vector in n directions. The maximal Lyapunov exponent λ_{max} is defined as the average growth rate of the separation vector between the nearby trajectories in the phase space. The inverse of λ_{max} is called Lyapunov time which is an average time-scale on which the system is chaotic, or the effective

prediction horizon. For non-chaotic system, the maximal Lyapunov exponent is negative (in which the nearby trajectories converge) or zero (the separation vector has a constant length as the system is periodic). A positive λ_{max} thus indicates chaos.

For low-dimensional systems, one can calculate λ_{max} by simply analyzing a sufficiently long time series of the dynamical signal [85]. This method involves constructing a system phase-space and finding the average rate at which the nearest neighbors diverge [86]. For DDEs, which are inherently infinite-dimensional equations due to the presence of the time delay, this method proves challenging because it is impossible to keep track of the growth rate of separation vector in all dimensions. In our system, we use the conventional method [28] which involves solving the linearized system equations to estimate λ_{max}.

The microwave time-delayed feedback loop system equation, we recall, is described by equation (3.12). We need to determine whether the points near solution $x(t)$ diverge as t increases. To do so, we perform a linearization about the solution $x(t)$ to see how the linear perturbation vector $\delta_x(t)$ changes as t increases. The linearized limit of equation (3.12) could be written as:

$$\frac{d\delta x}{dt} = -R\cos\big[x(t-1)\big]\delta x(t-1) \tag{3.28}$$

This equation is solved along with the system equation. Because this equation is linear in δx, the initial perturbation vector δx_0 could be generated as an unit-length vector without losing generality. If the trajectory $x(t)$ is chaotic then $\delta x(t)$ will approximately follow the relation $|\delta x| \sim e^{+\lambda_{max}t}$ which suggests that the growth

rate λ_{max} could be calculated as:

$$\lambda_{max} = \frac{1}{t} \ln \frac{|\delta x(t)|}{|\delta x(0)|} \tag{3.29}$$

Since the growth rate could be positive if $x(t)$ is chaotic, the solution $\delta x(t)$ may overflow. We overcome this by periodically re-normalizing the value of the growth vector to 1 by dividing $\delta x(t)$ by its magnitude. We then keep track of the magnitude:

$$\alpha_i = |\delta x(t_i)| \tag{3.30}$$

where t_i is the discrete timing, and computed as a number of time step Δt

$$t_i = i\Delta t \tag{3.31}$$

The calculation is repeated for a long enough time -after L iterations- so that the solution vector $x(t)$ will visit all the regions of system phase-space, thus we obtain the maximal Lyapunov exponent as [26]

$$\lambda_{max} = \frac{1}{L\tau} \sum_{i=1}^{L} \ln \alpha_i \tag{3.32}$$

3.3.2 Kaplan- Yorke Dimensionality

Besides describing by its positive maximal Lyapunov exponent, one can use a geometrical argument to illustrate the dynamical behavior of a chaotic system. This method includes interpreting differential equations as vector field and characterizing the dynamics in phase- space. Dissipative systems often have attractors. While rigorous mathematical definitions of attractors exist [25, 26, 28], a heuristic definition suffices for our discussion. An attractor is a subset of phase space with zero

volume, which is invariant under the dynamics of the system. This means that if the state of the system is on the attractor, the system will never leave the attractor. Attractors are associated regions of phase space with non-zero volume called basins of attraction. In the limit that time goes to infinity, the state of any system whose initial state was within the basin of attraction will approach the attractor. For chaotic systems, these attractors have fractal structure and non-integer dimension. Measuring this dimensionality quantifies the complexity of the chaotic system. It also has been shown that there is a relationship between the fractal dimension of a typical chaotic attractor and Lyapunov exponents [87, 88]. Let the set λ_i be the Lyapunov exponents of n-dimensional dynamical system, in which λ_i characterizes the growth rate of the ith separation vector in in phase space. The set is ordered in descending direction i.e., $\lambda_1 \geq \lambda_2 \geq ... \geq \lambda_n$ With K is the largest integer such that:

$$\sum_{i=1}^{K} \lambda_i \geq 0 \tag{3.33}$$

The Kaplan- Yorke dimension or Lyapunov dimension is then defined:

$$D_L = K + \frac{1}{|\lambda_{K+1}|} \sum_{i=1}^{K} \lambda_i \tag{3.34}$$

Due to the presence of delay, the delay differential equation is understood as an inherently infinite-dimensional problem. Numerous results however, indicate that the equation could have a discrete spectrum Lyapunov exponent and finite dimension attractors [87]. The method of calculating the dimensionality of chaotic attractors as computing the full Lyapunov spectrum, in the delay system is illustrated in [87]. After transforming the delay differential equation into N-dimensional mapping

by sampling the delay time at different intervals $\Delta t = \tau/(N-1)$, the Lyapunov exponents are computed using a method similar to that described in section 3.1 with N infinitesimal separation vectors $\delta x^i(t), 1 \leq i \leq N$. We start by selecting an initial separation vector. After iterating for a time tau, the vector is normalized to have length 1. Using the Gram-Schmidt procedure [26, 87], we normalize the second separation vector relative to the first, the third relative to the second, and so on. This procedure is repeated for L iterations then the exponent λ_i is calculated similarly to (3.32) as:

$$\lambda_{max} = \frac{1}{L\tau} \sum_{i=1}^{L} \ln \frac{|\delta x^i(k)|}{|\delta x^i(k-1)|} \tag{3.35}$$

After ordering the spectrum of Lyapunov exponents in descending direction, we use (3.34) to calculate the dimensionality to obtain the dimensionality of chaotic attractors.

Chapter 4: Dynamical Characteristics

In this chapter, we describe the dynamics of the microwave time-delayed feedback loop through numerical and analytical solutions as well as experimental measurements of the tuning voltage signals. The chapter is divided into two sections in which we discuss the dynamics of the system with two different nonlinearities: sinusoidal and Boolean (binary). For the case when the sinusoidal function is implemented, we simulate and experimentally observe the phase portrait at different values of the feedback strength R. We prove the existence of chaos in the system by calculating the maximal Lyapunov exponents and Kaplan-Yorke dimensionality. We discuss the broadband spectra of the chaotic tuning signal and the FM chaotic microwave signal. We also describe the route to chaos by constructing the bifurcation diagram recording the simulated and experimental time series of the tuning signal when R is smoothly varied. We created the Boolean (binary) nonlinearity by applying the threshold function to the sinusoidal relationship. When the sinusoidal function is replaced by this binary nonlinearity, the time-delayed feedback loop exhibits complex periodic behaviors and the bifurcation diagram shows an intricate self-similar structure. We also discuss the bifurcation diagram to show that the system has no fixed point solutions.

The simulated results were obtained by numerically integrating (3.12), starting from random initial conditions, using a 5^{th} order Dormand-Prince method with a constant step-size. The equation of motion used to model our feedback loop was pre-iterated for a sufficiently long time to eliminate any transient behavior associated with non-physical initial conditions. The experimental tuning voltage time series were observed and recorded on a digitizing oscilloscope. Additionally, we programmed the FPGA and auxiliary DAC channel to also produce a second output channel that corresponds to the signal immediately prior to the integrator, which allows us to simultaneously observe and plot the tuning voltage signal and its time derivative to create a two-dimensional phase-portrait of the dynamics.

Because the nonlinear function is periodic in x, the solutions to (3.12) are easily seen to be translationally invariant up to an integer multiple of 2π. That is, if $x(t)$ is a solution, then $x(t) + 2\pi m$ is also a solution, for any integer m. In practice, the voltage applied to the VCO is constrained to a limited range; we therefore choose to present here the dynamics of the system in the regime which the numerical solutions remain bounded within one cycle of the nonlinear function, with a peak-to-peak amplitude that is smaller than 2π. The dynamical behaviors of the tuning voltage in case of unbounded regimes will be discussed in chapter 5.

4.1 Sinuisoidal Nonlinearity

We discuss here the dynamical behaviors at different values of R of the tuning signal of the VCO when the sinusoidal nonlinear function is employed in the loop. In

Table 4.1: Summary of system parameters.

parameter	**value**
$F_s = 1/\Delta t$	15 Ms/s
k	600
τ	40 μs
A	0.2 V
γ	180 MHz/V
τ_d	10 ns
$\omega_0/2\pi$	3 GHz
α	0.0067 – 0.0175
R	1.5 – 4.20

experiment, to change the feedback gain R, we vary the integration proportionality constant α in (3.15) while keeping the feedback delay τ constant. This allows the dynamical timescale of the system to remain unchanged, while the feedback gain is increased. The parameter α can be adjusted to a precision of 40 bits by suitably programming the FPGA. A DC offset voltage was added to the output voltage from the DAC using a summing amplifier in order to keep the system within the linear tuning range of the VCO. Table 4.1 summarizes the parameters implemented in the experiment along with the value range of R used in mathematical model. As described in chapter 3, the system equation can be solved exactly using the lineariza-

tion technique when R is small enough. The results show that for $R \leq \pi/2$, the system exhibits the fixed point solutions at $x = 0$ and $x = \pi$. The stable fix point, $x = 0$, becomes unstable when $R = \pi/2$ as the system undergoes the Hopf bifurcation into the periodic regime. Fig. 4.1 illustrates the characteristic phase portraits obtained from experimental measurements and numerical simulations, showing the variety of behaviors of the system when $R \geq \pi/2$.

The periodic experimental time trace is displayed in Fig. 4.1(a) in which the period is estimated as four times of the feedback delay τ, 160 μs equivalent to the frequency of 6.25 kHz. The simulation and experiment phase-portrait both show the limit cycle which exhibits the point symmetry with respect to the origin. The system can also exhibit a different periodic state in Fig. 4.1(b), (e) and (h). The point symmetry is broken as the limit cycle splits into two coexisting cycles in phase portraits as shown in (e) and (h). Both of the coexisting limit cycles are symmetric to each other appearing as two "arms" inside the fundamental cycle. The time series shows qualitatively change in the shape of the waveform near the peaks of the sinusoidal function, both in the positive and negative slopes. These parts appear in all the cycles of the periodic behavior at a frequency of 13 kHz which is twice the system fundamental periodic frequency. The aperiodic behavior of the system is seen in Fig. 4.1 (c), (f) and (i) at $R = 4.176$, where the phase portraits become dense as more cycles fill in. Time series shows more and more unsmooth parts near extreme points appearing with frequencies as twice, four times and eight times the fundamental frequency of periodic behavior.

To show that the system exhibits chaotic behavior, we calculate the maxi-

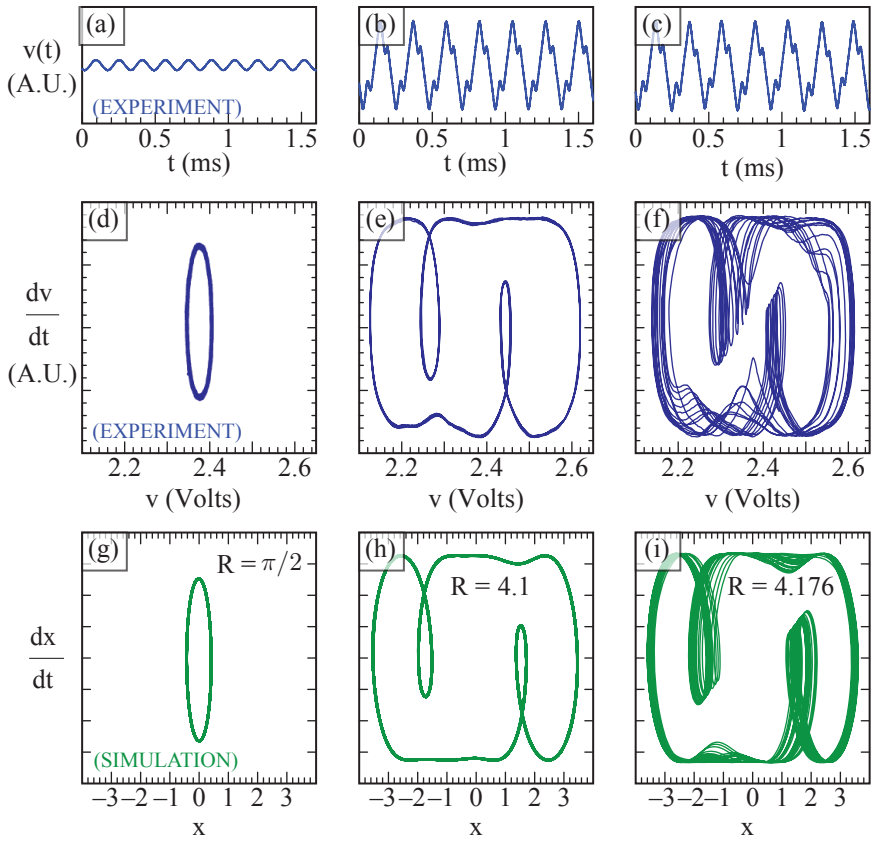

Figure 4.1: Phase portraits of the system recorded experimentally (top) and simulated numerically (bottom) as the normalized feedback gain R is varied.

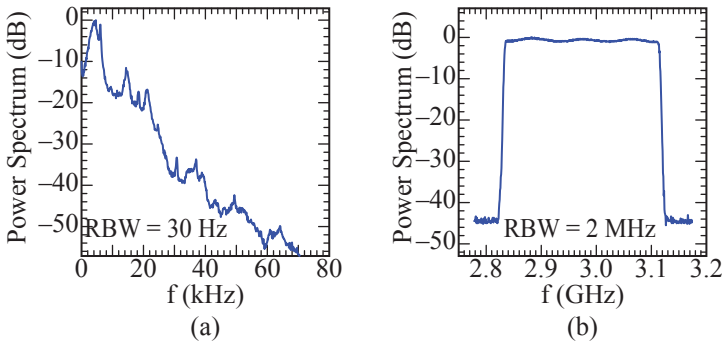

Figure 4.2: (a) Measured baseband power spectrum of the signal entering the VCO, $v(t)$, and (b) corresponding microwave spectrum of the resulting frequency-modulated signal. Both measurements were taken with $R = 4.176$, which produces chaotic dynamics. The resolution bandwidth (RBW) was 30 Hz and 2MHz for the baseband and microwave spectra, respectively, and both spectra were normalized relative to their maximum values.

mal Lyapunov exponents and Kaplan-Yorke dimensionality using the methods described in chapter 3. For the aperiodic behavior described in Fig.4.1(c), the maximal Lyapunov exponent $\lambda_{max} = +5.316/\tau$ indicating chaos; and K-Y dimensionality $D_{K-Y} = 2.15$ showing the fractal structure of the phase portrait. The baseband spectrum of the tuning voltage $v(t)$ and the corresponding microwave spectrum produced by the VCO, for the case of $R = 4.176$, are also plotted in Fig. 4.2. Because of the large tuning sensitivity of the VCO (γ in Table 4.1), the microwave signal occupies a much larger spectral bandwidth than the corresponding baseband signal. In this demonstration, the bandwidth of $v(t)$ was approximately 10 kHz and could be scaled to approximately 10MHz, at which point the dynamics would be constrained by the modulation bandwidth of the VCO. The microwave spectrum displays the broad band behavior which is ideal for communication applications.

The bifurcation diagrams of the tuning signal are shown in Fig. 4.3. The diagrams are created by calculating the color histogram of characteristic time traces as the feedback gain R is varied smoothly from 1.5 to 4.2. The experimental feedback gain R is varied by changing α in a fine resolution using a 40 bit binary number on FPGA. The proportionality between the integration factor α and the feedback gain R was inferred by empirically locating the value of α at which the first Hopf bifurcation occurs and associating this value with $R = \pi/2$. The process of constructing the diagram is described as following: For each value of R, we measured a time trace of the tuning voltage $v(t)$ and computed a normalized histogram of the voltage amplitudes. Each column of the bifurcation plot corresponds to a color-intensity plot of one such histogram.

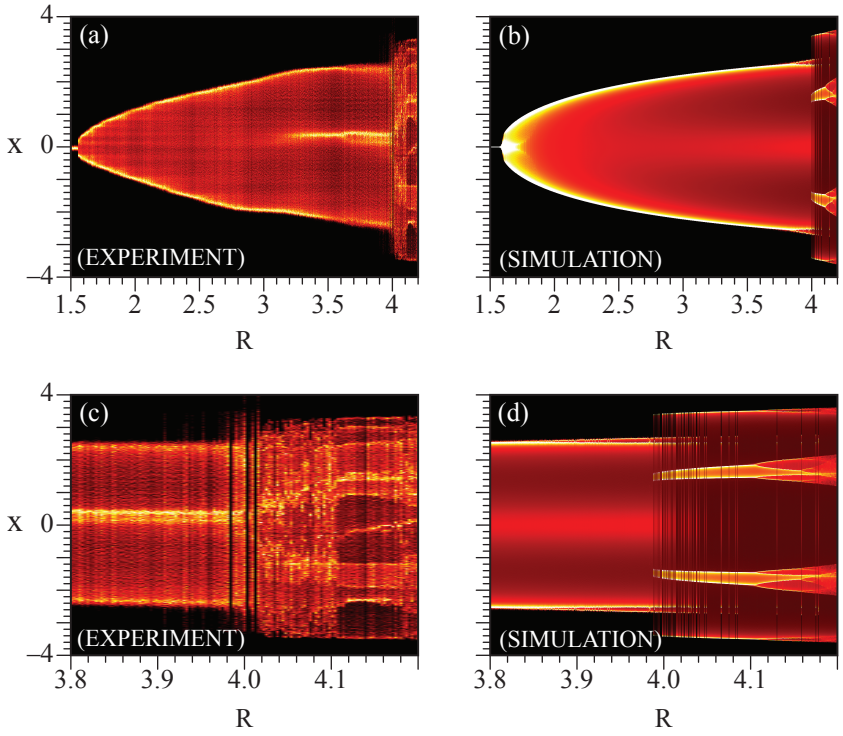

Figure 4.3: Bifurcation diagrams for the system with $1.5 \leq R \leq 4.2$ were constructed by calculating the color histogram of characteristic time traces. The experimental data were recorded using an 8-bit oscilloscope while the simulation results were obtained using Matlab.

Apart from scaling, there were no other adjustable parameters, and the theory exhibits good agreement with the experiment. In comparison to other time-delayed feedback systems in [43, 45, 65], the system exhibits periodic dynamics over most of the accessible range of feedback gains, with chaotic behavior only seen for a relatively narrow range of R. For $R \leq \pi/2$, it can be seen from the bifurcation diagram that the systems exhibits the steady state of fixed point behavior, $x = 0$. As R is increased, the system undergoes a series of bifurcations and displays increasingly complicated behavior ranging from periodic oscillations to chaotic dynamics. The periodic behavior appears at $R = \pi/2$, where the fixed point solution losses its stability. This behavior is characterized by two highly probable amplitude values in the bifurcation diagram. The amplitude of $x(t)$ increases with the feedback gain as phase portrait opens up. At $R = 3.9$, the bifurcation diagram shows an abrupt change, implying that the system makes a transition to a new dynamical regime. The amplitude values have more than two probable values, showing periodic behaviors in which more than one frequency co-exists. Increasing the feedback gain R leads to more coexisting cycles. At $R = 4.17$, the coexisting cycles become unstable and the system displays chaotic behavior. Fig. 4.3 (c) and (d) are zoomed-in bifurcation diagrams at nearby chaotic regimes when the feedback gain R is larger than 3.8. The diagrams show the system route to chaos is period- doubling, in agreement with to the numerical results presented in [78]. Close inspection of the bifurcation diagram obtained through simulation reveals that the system displays bi-stability. For a range of values of R, there are two coexisting attractors, one of which follows the period-doubling route to chaos as R is increased. The experimental bifurcation

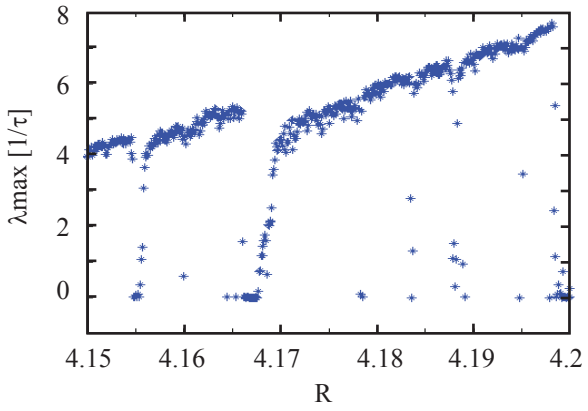

Figure 4.4: Maximal Lyapunov exponents for the system described in (3.12), as a function of the feedback gain, R.

diagram does not resolve this structure, in part due to the limited resolution of the DAC.

The maximal Lyapunov exponents for the system in aperiodic regime are also calculated numerically and presented in Fig. 4.4 in which the chaotic behaviors are indicated by positive values of λ_{max}.

4.2 Boolean Nonlinearity

An interesting and easily realized variation of this system is to replace the sinusoidal nonlinear function that relates v and w (c.f., Fig. 2.6) with a Boolean relationship. In practice, this could be achieved by simply inserting a digital threshold device (comparator) following the mixer, thereby producing either a positive or

negative output voltage of $w = \pm A$, depending on the sign of v. Experimentally, we achieve this by simply discarding all but the most significant (sign) bit during the analog-to-digital conversion of w. Mathematically, this nonlinearity may be modeled by replacing (3.7) by the Boolean relationship:

$$w(t) = A\,\mathrm{sgn}\Big(\cos\big[2\pi\gamma\tau_d v(t) - \omega_0\tau_d\big]\Big) \tag{4.1}$$

where sgn represents the algebraic sign function. In normalized time and amplitude units, the time-delayed dynamical equation becomes

$$\dot{x}(t) = -R\,\mathrm{sgn}\Big(\sin\big[x(t-1)\big]\Big) \tag{4.2}$$

$$= \begin{cases} +R, & \sin\left[x(t-1)\right] < 0 \\ -R, & \sin\left[x(t-1)\right] \geq 0 \end{cases} \tag{4.3}$$

where the single dimensionless constant R is defined as in (3.13).

Typical time traces along with time delay-embedding plots of $v(t)$ (or $x(t)$) are shown in Fig. 4.5. Unlike the earlier case, this system does not admit a fixed point solution for any value of R. Rather, the trajectories exhibit an alternating up-down sawtooth patterns that can be completely described by a sequence of switching times, i.e., the times at which the slope of $x(t)$ changes sign. These switching times can be calculated iteratively by locating the times at which $x(t-1)$ crosses a $m\pi$ threshold.

For values of $R \leq \pi$, the trajectories are symmetric triangular waves with a period of 4τ and a peak-to-peak amplitude of $2R$ centered about $x = 0$, as shown in Fig. 4.5(a,d,g). For $\pi \leq R \leq 4\pi/3$, the peak amplitude continues to grow

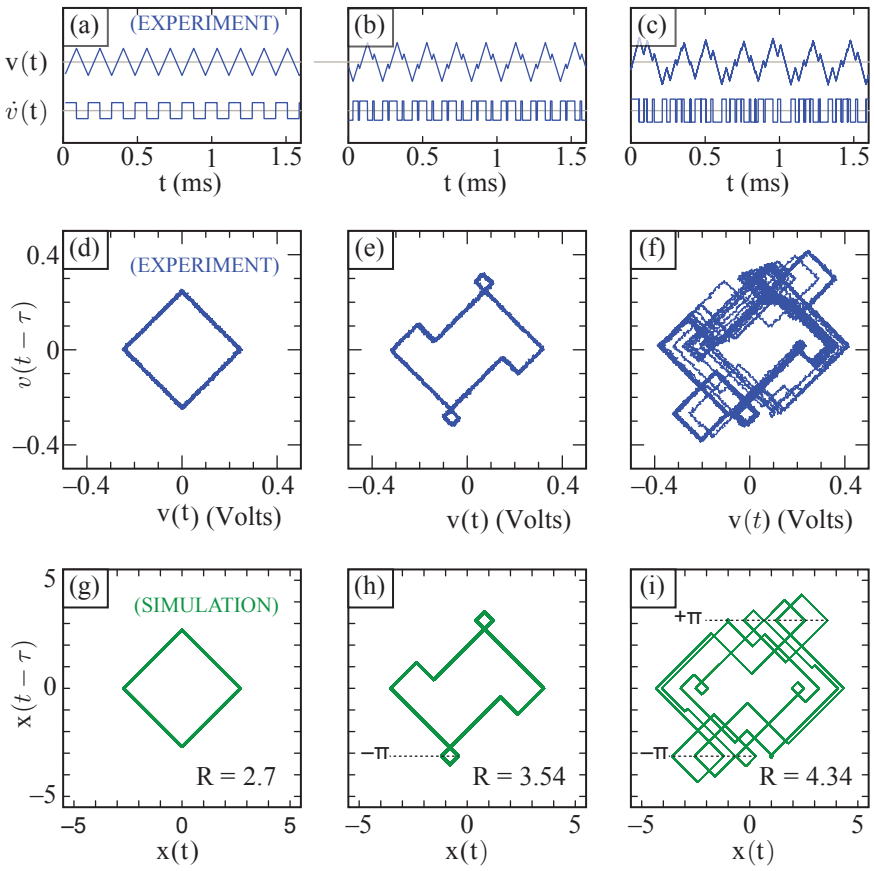

Figure 4.5: Experimental (blue) and simulated (green) time traces and time delay embedding plots of the system using Boolean nonlinearity at different values of normalized feedback gains R.

in proportion to R, but the trajectories acquire secondary peaks on the rising and falling edge of the triangular wave, as shown in Fig. 4.5(b,e,h). Above $R = 4\pi/3$, the behavior becomes more complicated, showing increasingly longer-period trajectories that depend very sensitively on the feedback gain R, as in Fig. 4.5(c,f,i). For all cases considered, the calculated dynamical behavior was observed to be periodic with an amplitude confined to the range $-R < x(t) < +R$, although the periodic orbits could contain as many as 54 segments, with periods approaching 60τ.

For $R \geq 3\pi/2$, the solutions no longer remain bounded, and $x(t)$ can instead exhibit a random-walk type behavior similar to what was observed for the sinusoidal case considered earlier. Even within this range, however, there exist isolated windows of R for which finite-amplitude solutions occur.

Fig. 4.6 presents a bifurcation diagram (experiment and simulation), showing the color-histogram of $x(t)$ as a function of the feedback gain R. Although the system is periodic for all points, the bifurcation diagram has a fractal characteristic in which any enlarged regions of the bifurcation appears self-similar to the original. This property is illustrated in Fig. 4.6(c) and Fig. 4.6(d), which show successive enlargements of the calculated bifurcation diagram.

While such a system can be classified as a continuous-time Boolean delay system, it does not fit the classic description of Ghil, for which the Boolean state depends only upon its prior value(s) [89]. Rather, in this case, the Boolean slope $\dot{x}(t)$ depends on a prior value of $x(t-1)$. The system shares some features in common with earlier systems that exhibit a switching nonlinearity [90], but it differs in that the dynamics are entirely characterized by the sequence of switching times.

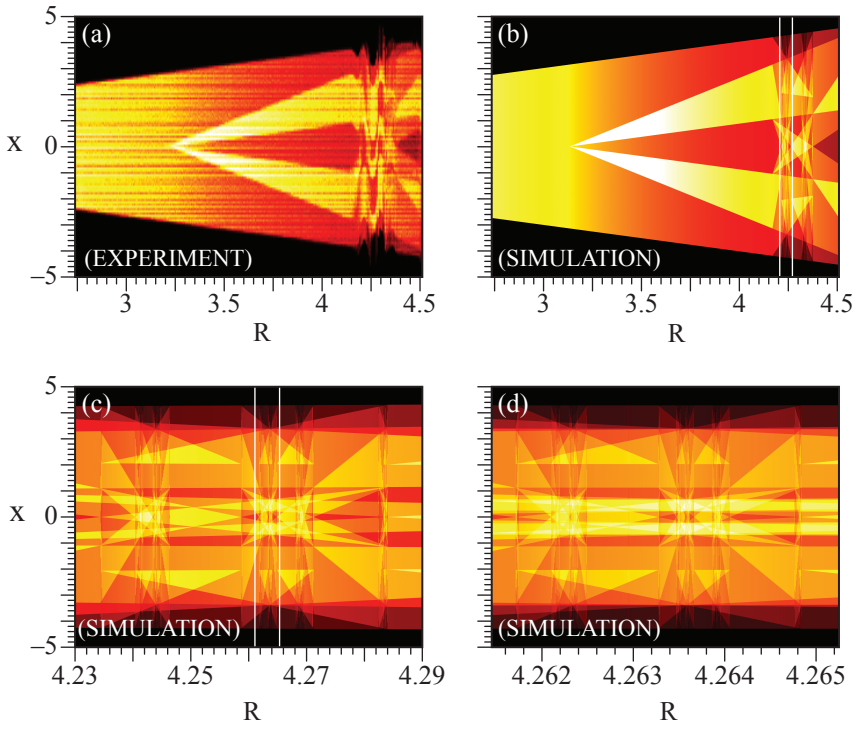

Figure 4.6: Bifurcation diagram of the system utilizing the Boolean nonlinearity when R is varied from 2.75 to 4.5. (a) Experiment, (b)(d) Simulation, showing fractal character of bifurcation digram, through successive enlargements of the bifurcation diagram.

The sawtooth waveforms generated by this system can have advantages for the frequency-modulated microwave system. The linear variation of the tuning frequency of the VCO produces a swept frequency signal with a linear chirp (positive or negative), which can simplify the signal processing for range-finding and Doppler velocity measurements.

Chapter 5: Deterministic Brownian Motion

Deterministic Brownian motion is defined as a Brownian motion produced from a deterministic process without the addition of noise. In this chapter, we discuss the existence of deterministic Brownian motion in the microwave time-delayed feedback loop when the system operates in the high feedback gain regime. We begin the discussion by a short description about the system setup, which consists of waveguide components to produce sinusoidal nonlinearity and a FPGA board to provide time delay and voltage integral functions. Numerical simulations of the system show behavior reveal that the system exhibits Brownian-like motion when the feedback gain is increases. The experimentally observed waveforms also display the properties of a random walk. We quantify the randomness by statistically finding the distribution function of the difference between the tuning voltages at two different times, separated by a fixed window time. We also estimate the Hurst exponents of the system experimentally and numerically using the method described in [25,28,91] to show that the system can exhibit different types of deterministic Brownian motions, depends on the value of the feedback gain R. The chapter concludes with the discussion of synchronization between Brownian motions when two such systems are unidirectionally coupled. We present the simulation results to show the range

of coupling strength in which two deterministic Brownian motions could synchronize; we also analyze the stability of the synchronization as a function of coupling strength and feedback gain. The possibility of having two synchronized random walks could have diverse applications ranging from modeling the stock market or resolving problem in financial systems [92].

5.1 Experimental Setup

The microwave time-delayed feedback loop used in this experiment is similar to the one we discussed in chapter 2, which comprises a nonlinear element, amplifier, time delay and filter. We again use a microwave homodyne phase discriminator to produce the sinusoidal nonlinearity and an FPGA board to program the digital delay and integrator. The system equation thus is the same as (3.12), but when the gain is increased, the solution $x(t)$ becomes unbounded and can traverse many cycles of the sinusoidal nonlinear function. In order to observe random-walk behaviors, the system was modified to increase the number of sinusoidal cycles that could be experimentally attained. Specifically, the VCO was replaced with a higher-frequency yttrium iron garnet (YIG) oscillator and the phase-delay in the homodyne phase discriminator was increased. The YIG oscillator is a different kind of tunable microwave source that, like the VCO, can produce microwave signals at high frequencies. The oscillator consists of an yttrium iron garnet (YIG) sphere mounted on a thermal conductive rod that is positioned inside of a magnetic field. The magnetic field could be created either by an electromagnet, or a permanent magnet, or a

combination of both. The magnetic field of an electromagnet can be "tuned using a variable current. The YIG sphere is a crystal that has a high Q characteristic which provides low phase noise and wide range frequency tuning (an order of multi-octave) in oscillators. Although YIG oscillator is not a compact microwave device, it offers several advantages over the normal VCOs, such as: broad band characteristic with linear tuning curve, low level of phase jitter, and stability to electronic noise. The YIG oscillator used in our system (Micro-Now 707 CW) could generate continuous wave frequencies from 2 to 120 GHz depending on the tuning voltage. The tuning range is 0 to 3.5 V with the tuning sensitivity of 2.3 GHz/V, and the tuning bandwidth is reported as 1.25 kHz. Similarly to the architecture described in chapter 2, the microwave signal after being generated by the YIG oscillator is sent to a 3 dB power splitter, phase delay, and homodyne mixer, which produces an output signal that is a sinusoidal function of the YIG frequency.

Since the output frequencies of YIG oscillator convey several microwave frequency bands, semirigid coaxial microwave cable is longer an ideal way to provide the delay between two signals coming out from the splitter. Instead, a K-band hollow rectangular waveguide is utilized in the system to create an appropriate low-loss delay amount without losing much energy at high frequency. In the setup, we use 2m long rectangular waveguide to create 15 ns delay. The signals are then sent to a double-balanced microwave mixer (Millitech- MXP 28A111L) [93]. This mixer offers low conversion loss and low noise figure over a wide range of IF and LO signals (26.5- 40 GHz). Other mixer features include high LO drive power- typically at 13 dBm, the LO/RF isolation is 15 dB; the LO/IF isolation is 20 dB depending on

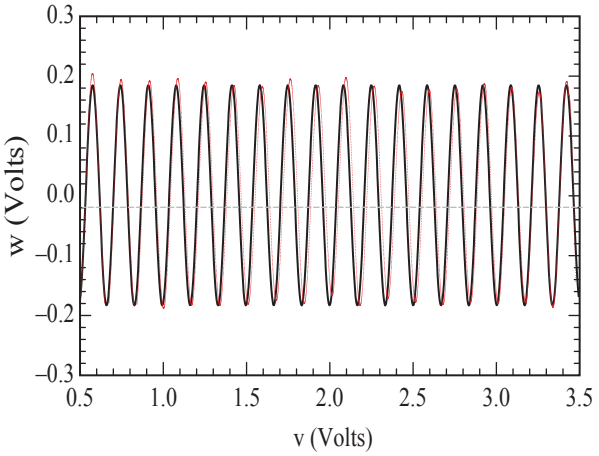

Figure 5.1: Measured nonlinearity (red) and the best fit sinusoidal function (black). The nonlinearity is produced by the homodyne phase discriminator consisting of a YIG oscillator, a 2m long waveguide and a double balanced mixer. The imperfections are due to the mixer electrical noise and the YIG thermal noise.

frequency scheme; the minimum 1dB compression point is 3 dBm.

Fig. 5.1 illustrates the nonlinearity produced by the YIG oscillator, a splitter, a 2 m long K-band waveguide and a double balanced mixer. The experimentally measured data is shown along with the best-fit sinusoidal function. The non-ideal features of the nonlinearity are due to the fluctuation to the operation temperature of the YIG and the mixer electrical noise.

The output of the mixer is sampled by the ADC fed to the FPGA, which implements the time delay and integration. The signal is finally converted back into

the analog form with the help of the DAC and connected back to the input of the YIG oscillator. The time delay has a constant value of 2 ms while the integration constant is controlled though a 40-bit binary number on the FPGA.

As before, the microwave time-delayed feedback loop can be modeled with the delay differential equation (3.12). The numerically computed and experimentally observed tuning voltage time traces are presented in the next section.

5.2 Deterministic Brownian Motion

In this section, we present experimental and simulation results of the system when it operates in the unbounded regime. In simulation, the delay differential equation is solved using the methods discussed in chapter 3. The numerical time trace is obtained by iterating the DDE equation starting from random initial conditions and iterating until transient behavior has died out.. In experiment, the time series is recorded using an 8-bit oscilloscope. Because the dynamical state of the random walk is unbounded, the output tuning voltage may eventually grow and surpass the range allowed by the DAC board. This will lead to either saturation of the output signals or rollover when the signal reaches the limit of the DAC. We overcome this problem by programming the FPGA to produce a logic pulse whenever the time-series saturates, which then causes the system to reset to the middle tuning voltage range. This method of collecting time traces is equivalent to repeating the solving process of the system equation with different random initial conditions.

Fig. 5.2(a) shows the experimentally measured tuning voltage time traces when

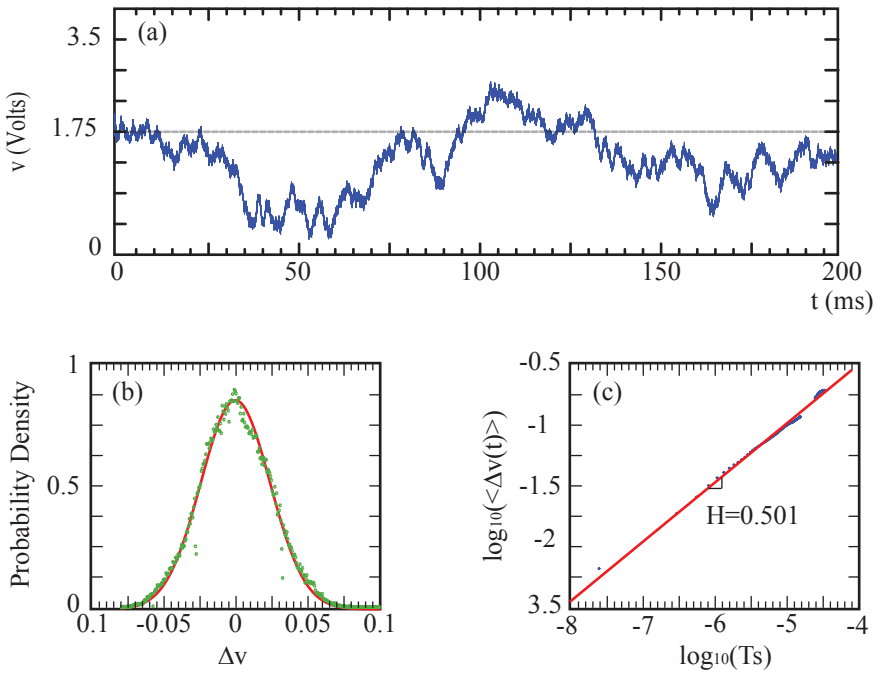

Figure 5.2: Experimental observed deterministic Brownian motion in microwave time-delayed feedback loop at feedback gain $R = 6.2$. (a). The fluctuation of tuning voltage time series about the initial offset level showing the dynamics behavior akin to the Brownian motion. (b) The probability distribution function of the displacement Δv. (c) Hurst exponent estimation from sliding the time window and calculate the average of absolute value of the displacement. The result shows that the tuning voltage dynamics is a regular Brownian motion with $H = 0.50$

the feedback gain R is set to approximately 6.2. The dynamics of the tuning signal resemble that of a Brownian particle, showing irregular trajectories irrespective of initial conditions. To quantify the Brownian nature, we examine the statistical properties of the time trace by calculating the statistical distribution function of the displacement $\Delta v = v(t) - v(0)$ as a function of the time interval t. The displacement Δv is computed by sampling the voltage at discrete times t_i, and computing $\Delta v_i = v_i - v_{i-1}$, where v_i is the value of the tuning signal at time t_i Fig. 5.2(b) shows the distribution function of Δv along with the best fit normal (Gaussian) distribution function.

To examine further the nature of the fluctuation in tuning voltage signal, we calculate the Hurst exponents for the system [25,28]. The Hurst exponent measures the smoothness of the time series with the value range from 0 to 1 with the higher values leading to a smoother motion. Hurst exponents also quantify the correlation between points in a time trace. If one consider pairs of points on a trace of a Brownian motion, separated by sample time T_s, the mean, absolute separation in $v(t)$ between points, i.e., $\langle|\Delta v|\rangle = \langle|v(t+T_s) - v(t)|\rangle$, is grows as a function of the time of separation:

$$\langle|\Delta v|\rangle \sim T_s^H \tag{5.1}$$

as H is Hurst exponent. The process of estimating H is adopted from [25, 91], and could be described as following. With the chosen time window of length T_s, we obtain the absolute value of the displacement $\Delta v(t)$ by sliding the time window from the beginning to the end of the time series. We then calculate the time average

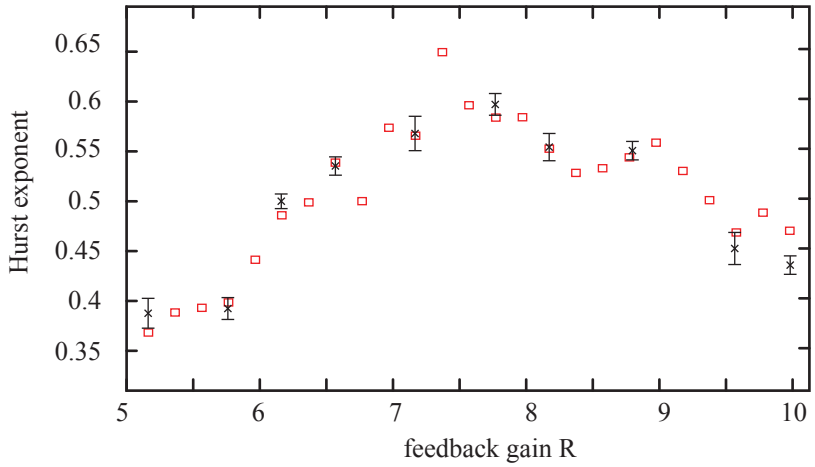

Figure 5.3: The Hurst exponent experimental estimated (black x with error bar) and numerically computed (red square) as a function of feedback gain R. The transition from anti-persistence to regular to persistence Brownian motion is shown.

value of the displacement $\langle|\Delta v|\rangle$. We next change the time windows length T_s and again compute the corresponding value of $\langle|\Delta v|\rangle$. Finally, we plot $\log(\langle|\Delta v|\rangle)$ versus $\log(T_s)$; if the plot appears as a straight line then the slope of the fit line is the Hurst exponent H of the time trace.

Fig. 5.2(c) illustrates the process of calculating the Hurst exponents for an experimental time series at the value of feedback gain $R = 6.2$. The Hurst exponent estimation data points, along with the fitted straight line are shown. We find that the tuning signal of the YIG oscillator in a microwave time-delayed feedback loop displays regular Brownian motion with a Hurst exponent $H = 0.50$.

The dependence of the system Hurst exponent H on the feedback gain R is presented in Fig. 5.3. The experimental estimated H are shown with error bars,

along with the simulation results. In experiment, for each value of feedback gain we record a data set by resetting the feedback loop to ensure that the output does not saturate. The plot shows that the system displays fractional Brownian motion whose Hurst exponent varies with the gain, taking values between 0.45 and 0.65. The system does not have a sudden transition in dynamics as the feedback gain is varied from 5 to 10. When the feedback gain R is below 6.2, the Hurst exponents have values less than 0.5. In this regime, the tuning voltage displays random dynamics, but the correlation between the data points is negative as the trace has a tendency to turn back upon itself. This behavior is termed anti-persistent Brownian motion. The Hurst exponent increases with the feedback gain. With the feedback range from 6.1 to 6.7, the system exhibits regular Brownian motion. When $6.7 \leq R \leq 9.4$, the Hurst exponents H are greater than 0.5, implying the system tuning voltage displays the persistent Brownian motion in which the tuning voltage traces become smoother and the increment between values at different times are positively correlated. When $R \geq 7.5$, H value decreases from 0.65 to less than 0.5 at $R = 10$.

5.3 Synchronization of Deterministic Brownian Motions

The time traces shown in section 5.2 are similar to the observed Brownian motion of small particles, therefore, provide an alternative way to understand the erratic phenomenon whose the physical descriptions are hard to establish. The concept of deterministic Brownian motion is also useful in modeling physical, biological behaviors that have stochastic aspects. We discuss here briefly the possibility of two

deterministic Brownian motions could proceed synchronously using the numerical model of the system.

We consider here two coupled feedback loops, as shown in Fig. 5.4 in which the systems are unidirectional coupled in a baseband, after the double- balanced mixer. Part of the mixer output from the master system is sent to the combiner to drive the slave system. In mathematical model of the coupled systems, we ignore the time delay in coupling path, and the coupling strength κ is normalized to be a dimensionless factor. We simulate the system starting from two uncoupled loops. After the master and slave systems have each reached the statistically stable regime (i.e., after the transient caused by random initial conditions has decayed) the coupling is turned on.

Before the coupling is turned on, each of the systems is governed by the same system equation of the time-delayed feedback in (3.12). After the coupling is taken place, the master system is modelled by the following equation:

$$\dot{x}_m(t) = -R\sin\big[x_m(t-1)\big] \tag{5.2}$$

While the equation for the slave system is:

$$\dot{x}_s(t) = -R\big[(1-\kappa)\sin\big[x_s(t-1)\big] + \kappa\sin\big[x_m(t-1)\big]\big] \tag{5.3}$$

where κ is coupling strength. The factor $(1-\kappa)$ in front of the slave system term ensures the existence of a synchronous solution, but doesn't guarantee that the synchronous state is stable.

The results of the coupled systems are obtained after waiting for the two systems to reach a stable behaviors. Fig. 5.5 display the evolution of $x(t)$ the before

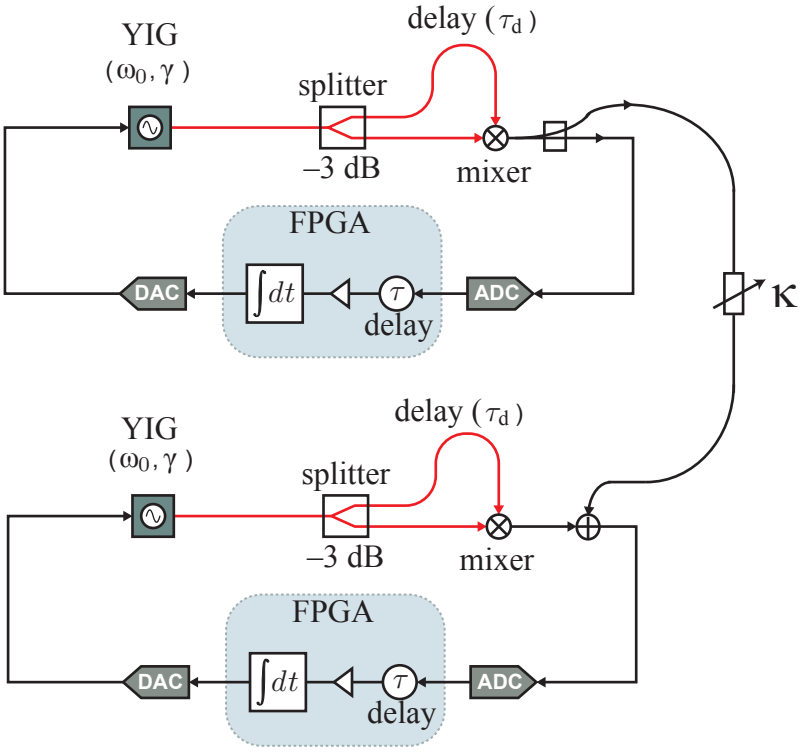

Figure 5.4: Coupling scheme of two microwave time-delayed feedback loops. The baseband signals are coupled with the mixer output signal is being transferred from the master system to the slave system.

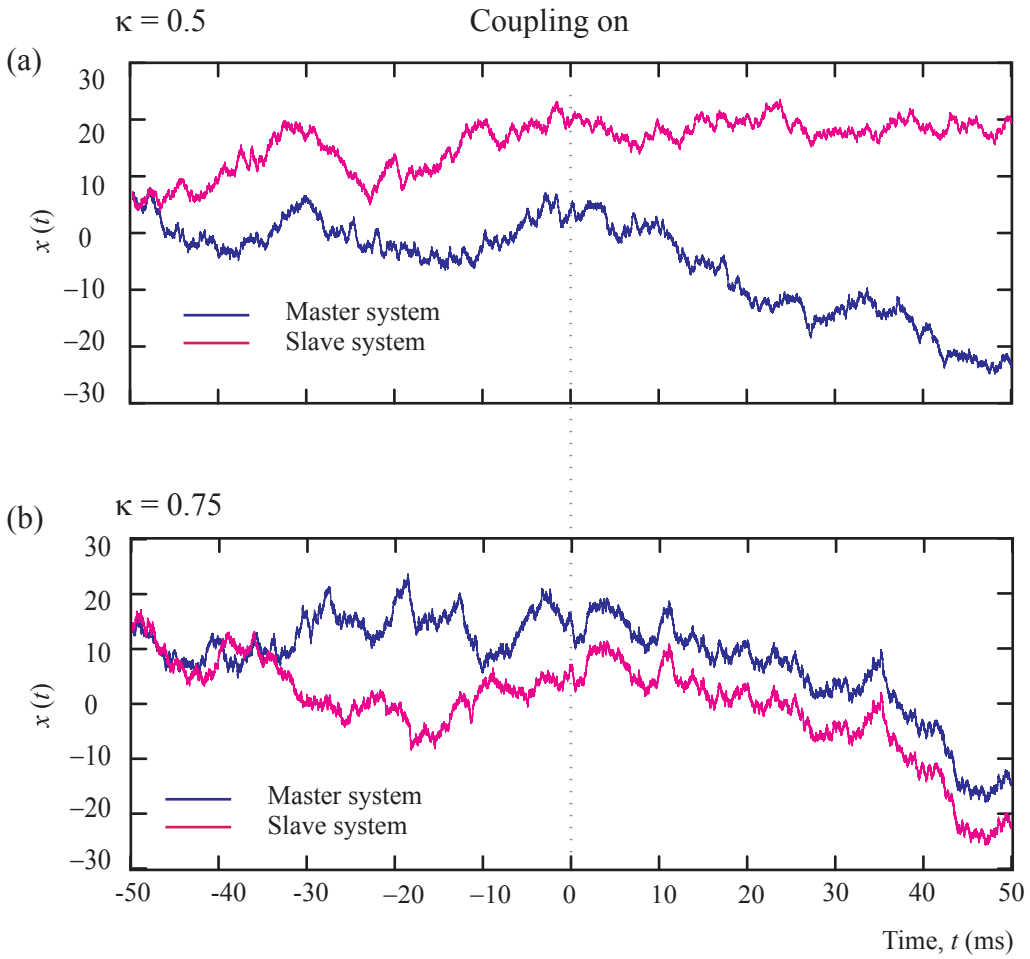

Figure 5.5: The coupled system at the feedback gain $R = 6.2$ at two different coupling strengths $\kappa = 0.5$ (a) and $\kappa = 0.75$ (b).

and after the coupling strength is turned on at the feedback gain$R = 6.2$. The simulation results are shown with two different coupling strength, $\kappa = 0.5$ and $\kappa = 0.75$. When $\kappa = 0.5$, as illustrated in Fig. 5.5(a), after the coupling turned on, two systems start to walk away from each other indicating there is no synchronization nor correlation between them. When $\kappa = 0.75$, we find that two Brownian motions start to walk parallel to each other not too long after the coupling is on. The offset between them is multiple integer number of 2π. This implies the master system drives the slave system to behave similarly even though their dynamics happens at two different cycles of nonlinearity.

To quantify the synchronization, we calculate the synchronization error as

$$\sigma = \sqrt{\left(\frac{\langle (x_{m-2\pi}(t) - x_{s-2\pi}(t))^2 \rangle}{\langle x_{m-2\pi}^2(t) + x_{s-2\pi}^2(t) \rangle} \right)}, \tag{5.4}$$

where $x_{m-2\pi}(t) = x_m(t) \bmod 2\pi$ and $x_{s-2\pi}(t) = x_s(t) \bmod 2\pi$. With this definition, $\sigma = 0$ when two deterministic Brownian motions exhibit the same dynamical behavior with an offset value of an integer multiple of 2π. The synchronization error as a function of coupling strength when the feedback gain $R = 6.2$ are plotted in Fig. 5.6. $\sigma = 0$ when the coupling strength is in the range from 0.75 to 0.8. With the coupling strength less than 0.75 or greater than 0.8, two systems are unsynchronized. It is also observed on the plot that the range of the synchronization dependent on the feedback gain R. Generally speaking, higher feedback gain leads to the more complex and random solutions, resulting in a smaller synchronization range.

We next investigate the stability of the synchronization solutions. While the stability of the synchronized solution of this system could be analyzed using the

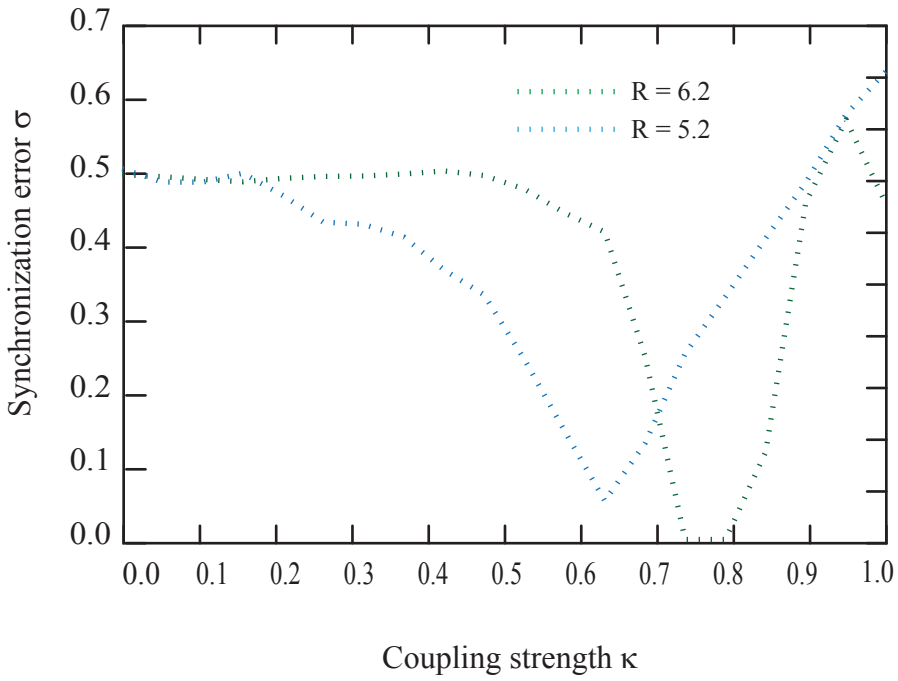

Figure 5.6: The synchronization error σ as a function of coupling strength κ. The synchronization range also depends on the feedback gain R.

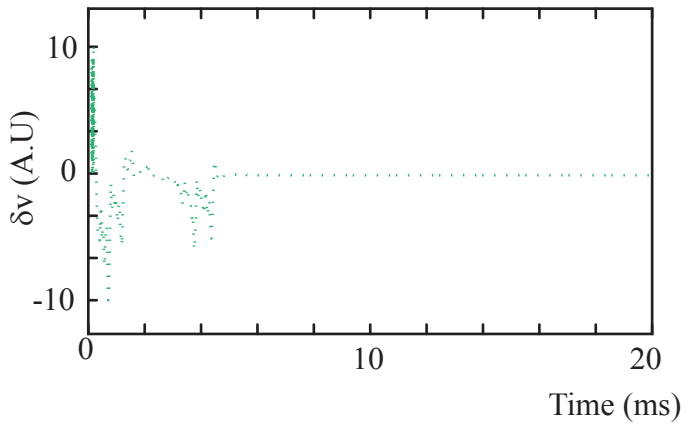

Figure 5.7: The synchronization perturbation vector δv converts to zero indicating the synchronization between two systems at $R = 6.2$ and $\kappa = 0.75$ is stable

master stability function formalism [94], this system does not have any complex network structure and a simpler linearization technique can be employed. When system is linearized about the synchronization solution by a small perturbation δx as $x_m = x_s + \delta x$, the goal is to check whether this perturbation vector dies out (unstable synchronized solution) or grows exponentially (unstable synchronized solution). The linearized equation for δx is found to be:

$$\dot{\delta}x(t) = -R(1-\kappa)\cos\big[x_m(t-1)\big]\delta x(t-1) \tag{5.5}$$

(5.5) is similar to the equation used to calculate the maximal Lyapunov exponents of the microwave time-delayed feedback loop. The solution of δv is obtained with a known state of x_m. Fig. 5.7 is the evolution of the synchronization perturbation vector δv when the feedback gain $R = 6.2$ and the coupling strength $\kappa = 0.75$. The

solution converges to zero after the transient time; the synchronization thus is stable

The experimental verification of the numerical works presented here can start by building two identical microwave time-delayed feedback loops. With the hybrid analog-digital setup of the loop, one can think of implementing the coupling function on the FPGA to have the flexibility of changing the coupling strength. The possible challenges of setting up coupled microwave time-delayed feedback loop come from matching two double-balanced mixers to have the same nonlinear properties.

The results presented in this section could be viewed as a starting point for a deeper exploration of the research on deterministic stochastic processes in time-delayed feedback loops. The concept of synchronization between random walks is interesting and applicable to various fields in science, technology and economics. There are a lot of works done about chaos synchronization [86, 95] which can be repeated to the synchronization between two or more deterministic Brownian motions.

Chapter 6: Conclusion

Nonlinear science has remained one of the most challenging and interesting fields of dynamics. The discovery of chaos had led to general interest of generating and utilizing chaotic signals for numerous applications, and has broadened our understanding of how complex dynamical systems work. The main subject of this thesis is a chaos generator in microwave frequency regime utilizing a time-delayed feedback loop architecture. The system is studied thoroughly using experimental measurements and numerical modelling to explore the dynamics behaviors inside and outside the bounded regime.

In chapter 2, we discussed in detail the main components that make up the microwave time-delayed feedback loop, presenting each component with its electrical properties and a mathematical description of its behavior. The experimental setup of the loop was also described, in which a time-delayed feedback loop was formed using a homodyne phase discriminator along with a delay and a voltage integrator on a field programmable gate array (FPGA) board. The homodyne phase discriminator is composed of commercially available microwave devices including a voltage controlled oscillator (VCO), 3 dB power splitter, semirigid microwave cable and a double-balanced mixer. The system is assembled on a microwave printed circuit board in

which connections between the devices are transmission lines designed to have a 50Ω impedance. The system produces a sinusoidal nonlinear function which serves as a nonlinearity of the time-delayed feedback loop. The delay and integrator functions are digitally programmed using a FPGA board. While we create the delayed function using a shift register, the summing accumulator is embedded on the FPGA processor to obtain the integral relationship. The microwave time-delayed feedback loop is thus a hybrid analog-digital system which provides flexibility in changing the system parameters.

We developed a mathematical model of the time-delayed feedback loop in chapter 3. The signal path was analyzed to obtain the system equation, which constitutes one of the simplest examples of a nonlinear time-delayed differential equation. We discussed analytical and numerical methods to solve this problem. The first Hopf bifurcation point is obtained by linearizing the system equation about its stationary solution. We also presented the method to quantify chaos by numerically calculating maximal Lyapunov exponent and Kaplan- Yorke (K-Y) dimensionality.

In chapter 4, the dynamics of the system in a bounded regime is discussed, and the experimental measurements are compared with numerical simulations. The system shows different dynamical behaviors ranging from a stable fixed point to a periodic to chaos depending on the value of the dimensionless feedback gain. The calculated maximal Lyapunov exponent and K-Y dimensionality show that chaotic behavior is present in the loop, when the feedback gain is sufficiently large. The route to chaos as frequency doubling is demonstrated using bifurcation diagrams. We also analyses the spectral properties of the signal, and confirm that it has a broad

spectrum which is demanded by many of the proposed technological applications of chaos. By reprogramming the sinusoidal nonlinearity with a simple threshold-based nonlinearity, we realized a Boolean dynamical system that shows a range of periodicities and fractal characteristics, depending on the feedback strength or time delay.

Chapter 5 was devoted to a discussion of deterministic Brownian motion in the microwave time-delayed feedback loop. We simulate the mathematical model and operate the experimental system in a higher gain regime to show the possibility of a deterministic Brownian motion. We use the distribution of displacements and the Hurst exponent to quantitatively study the deterministic Brownian motion. The numerically computed and experimentally estimated Hurst exponent values when the feedback strength is varied show that the system can exhibit the fractional Brownian motion, both anti-persistence and persistence behaviors. We consider the possibility of synchronization between two Brownian motions by simulating two feedback loops coupled unidirectional in the baseband. The results indicate that two deterministic Brownian systems can be synchronized such that they maintain the same fluctuation behavior, but with different offset levels. The allowable offset is constrained to be an integer number of 2π implying two systems are exhibiting identical deterministic Brownian motion at different cycles of sinusoidal nonlinearity. The synchronization range depends on the feedback gain as the higher feedback gain requires stronger coupling strength. We also prove the stability of the synchronization by numerically calculating the synchronization perturbation vector to show its convergence to zero.

6.1 Discussion: Application of Microwave Frequency-modulated Chaotic Signals

The microwave chaotic system presented here is well modeled using nonlinear delay differential equation and shows by excellent agreement between simulation and experiment, as described in chapter 4. The work described here could be explored for any time-delayed feedback loop with any filter function and nonlinearity which is associated to sinusoidal function. As we mentioned in chapter 4, due to the simplicity of the integral function, the system exhibits a narrower chaotic window compared with other time-delayed feedback loops that involve, for example, band-pass of low-pass filters [96].

With the VCO acting like a frequency modulator in the loop, the system can generate the microwave frequency modulated (FM) chaotic signal where the tuning voltage is deterministic and aperiodic. Unlike amplitude chaos signals, this chaotic frequency- fluctuated signals could offer many advantages over the continuous wave in communication applications, such as less susceptibility to noise or jamming, less power consumption at higher frequency, and greater signal-to-noise performance . The chaotic FM signal also potentially find applications in ranging and radar systems, which could benefit from the broadband noise-like nature of the signal. The aperiodicity of a chaotic FM signal can provide lower probability of detection or interception and reduces the susceptibility to interference from/with other microwave channels. We describe here the idea of chaotic radar utilizing the microwave FM

chaotic signal as a transmitted signal. This FM chaotic signal was generated from a microwave time delayed feedback loop whose filter function is one-pole low-pass filter [96].

To consider the effectiveness of this chaotic FM signal in target detection, we compute the ambiguity function of the microwave chaotic signal:

$$\chi(\tau, f) = \int_{-\infty}^{+\infty} s(t)s^*(t-\tau)e^{-i2\pi f\tau}dt \tag{6.1}$$

where $s(t)$ is the frequency-modulated microwave signal,

$$s(t) = \exp\left(i2\pi\gamma \int v_{\text{tune}}(t)dt\right) \tag{6.2}$$

and γ is the tuning coefficient of the VCO (typically given in MHz/V).

The ambiguity function is a two-dimensional function of τ and f,which represent how well one can resolve time-delay and Doppler shift of the reflected signal, respectively. The ambiguity function thus provides information about how well a matched receiver can unambiguously measure the range (τ) and velocity (f) of a signal [97]

Fig. 6.1 shows a contour plot of the magnitude $|\chi(\tau, f)|$, illustrating the advantages of using a chaotic FM signal in range and velocity sensing. Fig. 6.1(a) was obtained by using a continuous-wave microwave signal (i.e., v_{tune} = constant), for which the range cannot be unambiguously determined, as expected. Fig. 6.1(b) was obtained using a periodic v_{tune}, in which case the Doppler shift (f) can be more accurately estimated, and the position can also be determined. Because the modulation is periodic (with a period of approximately 4 μs), the range can only be determined up to an additive integral multiple of 4 μs. Fig. 6.1(c) was obtained using a larger

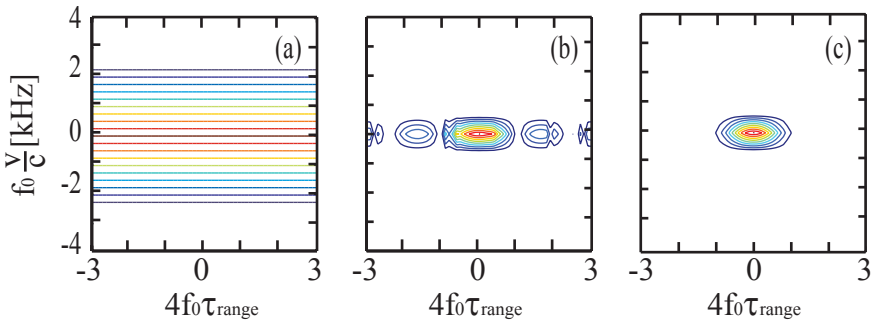

Figure 6.1: The calculated ambiguity functions of the continuous waveform (a), a periodic FM signal (b) and a chaotic FM signal (c). The function is calculated using Fourier transform with center frequency f_0 on complex signals as velocity and the range of the target are varied.

feedback strength, for which the modulation is chaotic. In this case, the system is predicted to yield more precise and unambiguous measurement of both range and velocity.

6.2 Proposed Future Research

6.2.1 Frequency Locking (Phase Synchronization) in FM Chaotic Signals

A surprising aspect of chaos is that despite the aperiodic nature and sensitive dependence on initial conditions characteristics, two chaotic systems can be synchronized, when they are appropriately coupled [98]. Synchronization of chaos is an interesting phenomena with great applications in many fields of science and

technology. The study of synchronization leads to a better understanding of collective behaviors in nature, such as the motion of school fish or the flashing in unison of fireflies. Chaotic synchronization is widely used in secure communications, weather prediction, parameter estimation and sensing networks. The microwave time-delayed feedback loop here could be viewed as a chaotic generator providing different type of chaotic signals: amplitude chaos in baseband frequency and frequency-modulated chaos in microwave frequency. The two feedback loops could be coupled in baseband or microwave bandwidths promising two possible types of chaos synchronization: the envelope synchronization between two tuning signals and phase synchronization (phase locking) between two microwave chaotic FM signals (in which two signals are also locked in phase). Fig. 6.2 demonstrates the coupling scheme in the microwave frequency of two microwave time-delayed feedback loops. The information from microwave signals coming out of the VCOs is shared between two systems.

While most of the past research has dealt with the baseband amplitude chaos synchronization, the study of phase looking between two phase chaotic signals deserves additional study. The phase locking phenomenon of FM chaotic signals could offer advantages in radio, telecommunications, GPS, satellite communication and radar applications due to the complex, aperiodic and high frequency features. It also could be used to demodulate a noisy signal from communication channels or distribute precisely timed clock pulses in digital logic circuits. As a chaotic FM signal generator, the microwave time-delayed feedback loop is useful for experimental and theoretical research on the interesting phase locking behavior.

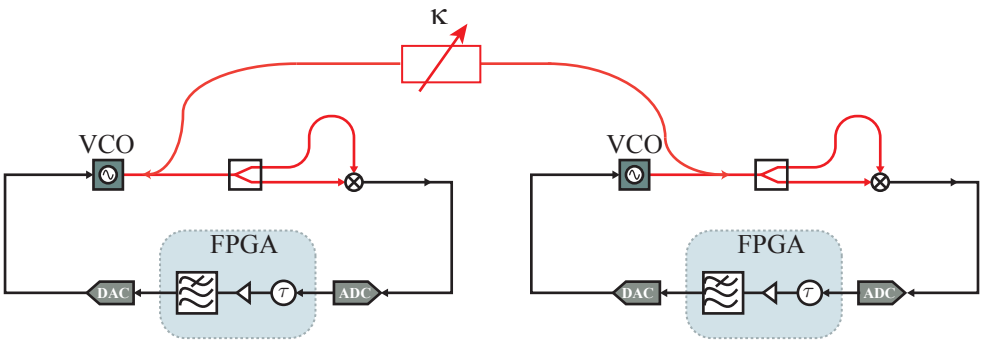

Figure 6.2: The coupling scheme of between two microwave time-delayed feedback loops in microwave bandwidth. The information from the microwave signals coming out of the VCOs is shared between two systems.

6.2.2 Network of Periodic Oscillators

We also discussed the time-delayed feedback loop when it was incorporated with binary nonlinear function. The good agreement between simulation and experiment suggest the application of the system in studying networks of periodic oscillators. Implementing a large network in practice is challenging because one has to maintain the coupling between nodes while keeping each node's features unchanged. The FPGA in the microwave time-delayed feedback loop could be used to program the coupling function and frequency of periodic oscillator (by changing the time delay). The hybrid setup of the microwave time-delayed feedback system allows individuals to change the topology of the network and properties of each oscillator

in an easy, convenient way. Furthermore, one can think of using a digital microwave devices to create homodyne phase discriminator on a FPGA board to form a compact dynamical system. The setup offer a promising experimental system for a high demand research area in complex networks.

6.2.3 The Feedback Loop with Multiple Time Delay

Incorporating the FPGA board in the system also makes it easy to change the feedback delay. There have been many of theoretical papers that consider the effect of time delay in dynamical systems [99–105]. The experimental research can take place by using the system demonstrated in this thesis with modified time delay function. By programming the FPGA, one not only can change the amount of delay time but also implementing multiple delay functions, with different statistical distributions, in the loop. The large memory of a FPGA allows those modifications done in a great range of values.

Bibliography

[1] H. Poincaré. *Sience and Method*. Nelson, New York, 1914.

[2] E. N. Lorenz. Deterministic nonperiodic flow. *Journal of Atmospheric Sciences*, 20:130–141, 1969.

[3] D. Kaplan and L. Glass. *Understanding Nonlinear Dynamics*. Springer, 1995.

[4] H. L. Swinney and J. P. Gollub. *Hydrodynamic Instabilities and the Transition to Turbulence*. Springer, 1981.

[5] Y. Kuramoto. *Chemical Oscillations, Waves, and Turbulence*. Dover Publications, New York, NY, 2003.

[6] R. Blumel. *Chaos in Atomic Physics*. Cambridge University Press, 1997.

[7] D. L. Turcotte. *Fractals and Chaos in Geology and Geophysics*. Cambridge University Press, 1997.

[8] G. Mazzini, R. Rovatti, and G. Setti. Interference minimisation by autocorrelation shaping in asynchronous ds-cdma systems: Chaos-based spreading is nearly optimal. *Electron. Lett.*, 35(13):1054–1055, 1999.

[9] J.H.B. Deane and D.C. Hamill. Improvement of power supply emc by chaos. *Electronics Letters*, 32(12):1045, 1996.

[10] L. Fortuna, M. Frasca, and A. Rizzo. Chaotic pulse position modulation to improve the efficiency of sonar sensors. *IEEE Trans. Instrum. Meas.*, 52(6):1809–1814, 2003.

[11] J. Paul, S. Sivaprakasam, and K. Alan Shore. Dual-channel chaotic optical communications using external-cavity semiconductor lasers. *J. Opt. Soc. Am. B*, 21(3):514–521, 2004.

[12] A. Argyris, D. Syvridis, L. Larger, V. Annovazzi-Lodi, P. Colet, I. Fischer, J. García-Ojalvo, C. R. Mirasso, L. Pesquera, and K. A. Shore. Chaos-based communications at high bit rates using commercial fibre-optic links. *Nature*, 438:343–346, 2005.

[13] K.M. Cuomo, A.V. Oppenheim, and S.H. Strogatz. Synchronization of lorenz-based chaotic circuits with applications to communications. *IEEE Trans. Circuits Syst. II, Analog Digit. Signal Process.*, 40(10):626–633, 1993.

[14] G. D. VanWiggeren and R. Roy. Communication with chaotic lasers. *Science*, 279(5354):1198–1200, 1998.

[15] G.M. Bernstein and M.A. Lieberman. Secure random number generation using chaotic circuits. *IEEE Trans. Circuits Syst.*, 37(9):1157–1164, 1990.

[16] J. T. Gleeson. Truly random number generator based on turbulent electro-convection. *Appl. Phys. Lett.*, 81:1949, 2002.

[17] T. Stojanovski and K. Ljupčo. Chaos-based random number generators – part i: Analysis. *IEEE Trans. Circuits Syst. I*, 48(3):281–288, 2001.

[18] T. Stojanovski, J. Pihl, and K. Ljupčo. Chaos-based random number generators – part ii: Practical realization. *IEEE Trans. Circuits Syst. I*, 48(3):382–385, 2001.

[19] A. Uchida, K. Amano, M.i Inoue, K. Hirano, S. Naito, H. Someya, I. Oowada, T. Kurashige, M. Shiki, S. Yoshimori, K. Yoshimura, and P. Davis. Fast physical random bit generation with chaotic semiconductor lasers. *Nature Photon.*, 2:728–732, 2008.

[20] K. Myneni, T. A. Barr, B. R. Reed, S. D. Pethel, and N. J. Corron. High-precision ranging using chaotic laser pulse train. *Appl. Phys. Lett.*, 74:1496–1498, 2001.

[21] B.C. Flores, E.A. Solis, and G. Thomas. Assessment of chaos-based fm signals for range-doppler imaging. *IEE Proc. Radar Sonar Navig.*, 150(4):313–322, 2003.

[22] F. Lin and J-M. Liu. Chaotic radar using nonlinear laser dynamics. *IEEE J. Quantum Electron.*, 40(6):815–820, 2004.

[23] T. L. Carroll. Chaotic system for self-synchronizing doppler measurement. *Chaos*, 15:013109, 2005.

[24] M. C. Mackey and L. Glass. Oscillation and chaos in physiological control systems. *Science*, 197(4300):287–289, 1977.

[25] P.S. Addison. *Fractals and Chaos: An illustrated course*. IOP Publishing Ltd, first edition, 1997.

[26] E. Ott. *Chaos in Dynamical Systems*. Cambridge University Press, Cambridge, U. K., second edition, 2002.

[27] T. Erneux. *Applied Delay Differential Equations*. Springer, first edition, 2009.

[28] J. C. Sprott. *Chaos and Time-series Analysis*. Oxford University Press, first edition, 2003.

[29] S. Thompson. Delay differential equations. *Scholarpedia*, 2(3):2367, 2007.

[30] E. Ggrigorieva, H. Haken, A. A. Kashchenko, and A. Pelster. Travelling wave dynamics in a nonlinear interferometer with spatial field transformer in feedback. *Physica D*, 125:123, 1999.

[31] S. E. Kingsland. *Modeling Nature: Episodes in the History of Population Ecology*. University of Chicago Press, 1985.

[32] W. S. C Gurney, S. P. Blythe, and R. M. Nisbet. Nicholson's blowflies revisited. *Nature*, 287:17–21, 1980.

[33] K. Ikeda, H. Daido, and O. Akimoto. Optical turbulence: Chaotic behavior of transmitted light frin a ring cavity. *Phys. Rev. Lett*, 45:709–712, 1980.

[34] L. Larger, J. P. Goedgebuer, and J. M. Merolla. Chaotic oscillator in wavelength: A new setup for inverstigating differential difference equations describing nonlinear dynamics. *IEEE J. Quant. Electron.*, 34:594–601, 1998.

[35] P. Mandel. *Theoretical Problems in Cavity Nonlinear Optics*. Cambridge UniversityPress, 1997.

[36] E. Villermaux. Pulsed dynamics of foutains. *Nature*, 371:24–25, 1994.

[37] E. Villermaux. Memory-induced low frequency oscillations in closed convection boxes. *Phys. Rev. Lett*, 75:4618–4621, 1995.

[38] R. J. Henry, Z. N. Masoud, A. H. Nayfeh, and D.T. Mook. Cargo pendulation reduction on ship-mouted crabes via boom-lu angle actuation. *J. Vibration Control*, 7:1253–1264, 2001.

[39] Z. N. Masoud, A. H. Neyfeh, and A. Al-Mousa. Delayed position feedback controller for the reduction of payload pendulations of rotary cranes. *J. Vibration Control*, 9:257–277, 2003.

[40] Z. N. Masoud, A. H. Neyfeh, and N. A. Neyfeh. Sway reduction on quayside container cranes using delayed feedback controller. *J. Vibration Control*, 35:1103–1122, 2005.

[41] M. Szydlowski and A. Krawiec. Scientific cycle model with delay. *Scientometrics*, 52:83–95, 2001.

[42] M. Kalecki. A macrodynamic theory of business cycle. *Econometrica*, 3:327–344, 1935.

[43] A. B. Cohen, B. Ravoori, T. E. Murphy, and R. Roy. Using synchronization for prediction of high-dimensional chaotic dynamics. *Phys. Rev. Lett.*, 101:154102, 2008.

[44] J. N. Blakely, L. Illing, and D. J. Gauthier. High-speed chaos in an optical feedback system with flexible timescales. *IEEE J. Quantum Electron*, 40:299–305, 2004.

[45] L. Illing and D. J. Gauthier. Hopf bifurcation in time-delay systems with band-limited feedback. *Physica D*, 210:180–202, 2005.

[46] J. C. Maxwell. *A Treatise on Electricity and Magnetism*. Dover, N. Y, 1954.

[47] A. A. Oliner. Historical perspectives on microwave field theory. *IEEE Trans. Microwave Theory and Techniques*, MTT-32:1022–1045, 1984.

[48] D. M. Pozar. *Microwave Engineering*. John Wiley & Sons, second edition, 1998.

[49] S. V. Marshall and G. G. Skitek. *Electromagnetic Concepts and Applications*. Prentice- Hall, third edition, 1990.

[50] C. A. Balanis. *Advanced Engineering Electromagnetics*. John Wiley & Sons, 1989.

[51] S. R. Theodore. *Wireless Communications: Principles and Practice*. Prentice-Hall, second edition, 2002.

[52] A. Einstein. *Investigations of the Theory of Brownian Movement*. Dove, 1956.

[53] N. Wiener. Differential space. *Journal of Mathematical Physics*, 2:131–174, 1923.

[54] G. H. Wannier. *Statistical Physics*. Wiley, New York, first edition, 1966.

[55] C. Beck. Higher correlation functions of chaotic dynamical system - a graph theoretical approach. *Nonlinearity*, 4:1131, 1991.

[56] R. Klages and N. Korabel. Understanding deterministic diffusion by correlated random walks. *J. Phys. A*, 35:4823, 2002.

[57] G. Trefán, P. Grigolini, and B. J. West. Deterministic brownian motion. *Phys. Rev. A*, 45:1249–1252, 1992.

[58] P. Gaspard, M. E. Briggs, M. K. Francis, J. V. Sengers, R. W. Gammon, J. R. Dorfman, and R. V. Calabrese. Experimental evidence for microscopic chaos. *Nature*, 394:865–868, 1998.

[59] M. Romero-Bastida and E. Braun. Microscopic chaos from brownian motion in a one-dimensional anharmonic oscillator chain. *Phys. Rev. E*, 65:036228, 2002.

[60] M. Romero-Bastida, D. Casta neda, and E. Braun. Macroscopic evidence of microscopic dynamics in the fermi-pasta-ulam oscillator chain from nonlinear time-series analysis. *Phys. Rev. E*, 71:046207, 2005.

[61] L.Y. Chew and C. Ting. Microscopic chaos and gaussian diffusion processes. *Physica A: Statistical Mechanics and its Applications*, 307(34):275 – 296, 2002.

[62] M. C. Mackey and M. T-Kamiska. Deterministic brownian motion: The effects of perturbing a dynamical system by a chaotic semi-dynamical system. *Physics Reports*, 422(5):167 – 222, 2006.

[63] J. Lei and M. C. Mackey. Deterministic brownian motion generated from differential delay equations. *Phys. Rev. E*, 84(14):041105, 2011.

[64] K. Ikeda and K. Matsumoto. High-dimensional chaotic behaviors in systems with time-delayed feedback. *Physica D*, 29:223–235, 1987.

[65] L. Illing and D. J. Gauthier. Ultra-high-frequency chaos in a time-delay electronic device with band-limited feedback. *Chaos*, 16:033119, 2006.

[66] Y. C. Kouomou, P. Colet, L. Larger, and N. Gastaud. Chaotic breathers in delayed electro-optical systems. *Phys. Rev. Lett.*, 95:203903, 2005.

[67] Mini-Circuits, Inc. *Surface Mount Voltage Controlled Oscillator SOS-3065-119+*, rev. or m122533 edr-8384/1 f1 edition.

[68] R. E. Collin. *Foudations for Microwave Engineering.* Wiley- Interscience, second edition, 2000.

[69] Marki Microwave, Inc. *Mixer Basic Primer*, first edition, 2010.

[70] Mini-Circuits, Inc. *Understanding Mixers- Terms Defined and Measuring Performance*, an-00-009 rev.: or m117160 edition, June.

[71] Mini-Circuits, Inc. *Ceramic Frequency Mixer Wide Band MCA1-80LH+*, rev. bm102713 ed-11119 edition.

[72] B. C. Wadell. *Transmission Line Design Handbook.* Artech Print, 1991.

[73] National Semiconductor. *ADC8200 8-Bit, 20 Msps to 200 Msps, Low Power A/D Converter with Internal Sample-and-Hold*, 200179 edition, February.

[74] Texas Instruments. *10-Bit, 165 Msps Digital-to-Analog Converter*, sbas093b edition, May.

[75] KNJN LLC. *KNJN FX2 FPGA Development Boards*, r92 edition, November.

[76] R. E. Simpson. *Introductory Electronics for Scientists and Engnieers*. Allyn and Bacon, second edition, 1987.

[77] J. C. Sprott. A simple chaotic delay differential equation. *Phys. Lett. A*, 366:397–402, 2007.

[78] M. Schanz and A. Pelster. Analytical and numerical investigations of the phase-locked loop with time delay. *Phys. Rev. E*, 67:056205, 2003.

[79] H. Dao, J. C. Rodgers, and T. E. Murphy. Chaotic dynamics of a frequency-modulated microwave oscillator with time-delayed feedback. *Chaos*, 23:013101, 2013.

[80] L. F. Shampine and S. Thompson. Solving delay differential equation with dde23. *Tutorial*, 2000.

[81] C. Marriott and C. Delisle. Effects of discontinuities in the behavior of a delay differential equation. *Physica D*, 36:198–206, 1989.

[82] C. T. H. Baker, C.A.H.Paul, and D.R. Willé. A bibliography on the numerical solution of delay differential equations. *Numer. Anal. Rept.*, 269, 1995.

[83] S. H. Strogatz. *Nonlinear Dynamics and Chaos*. Perseus Books Publishing, 1994.

[84] W. Wischert, A. Wunderlin, A. Pelster, M. Olivier, and J. Groslambert. Delay-induced instabilities in nonlinear feedback systems. *Phys. Rev. E*, 49(1):203–219, 1994.

[85] H. D. I. Abarbanel. *Analysis of Observed Chaotic Data*. Springer, 1995.

[86] A. B. Cohen. *Synchronization and Prediction of Chaotic Dynamics on Networks of Optoelectronic Oscillators*. PhD thesis, University of Maryland, College Park, USA, 2011.

[87] J. D. Farmer. Chaotic attractors of an infinite-dimensional dynamical system. *Physica D*, 4(3):366–393, 1982.

[88] J. L. Kaplan and J. A. Yorke. Chaotic behavior of multidimensional difference equations. *Functional Differential Equations and Approximations of Fixed Points*, 730:204, 1979.

[89] M. Ghil, I. Zaliapin, and B. Coluzzi. Boolean delay equations: A simple way of looking at complex system. *Physica D*, 237:2967–2986, 2008.

[90] N. J. Corron, J. N. Blakely, and M. T. Stahl. A matched filter for chaos. *Chaos: An Interdisciplinary Journal of Nonlinear Science*, 20(2):023123, 2010.

[91] W-S. Lam, W. Ray, P. N. Guzdar, and R. Roy. Measurement of hurst exponents for semiconductor laser phase dynamics. *Phys. Rev. Lett.*, 94:010602, 2005.

[92] R. N. Mantegna and H. E. Stanley. *Introduction to Econophysics: Correlations and Complexity in Finance*. Cambridge University Press, 2000.

[93] Millitech. *Serries MXP Balanced Mixer*, is000031 rev 03 edition, February.

[94] L. M. Pecora and T. L. Carroll. Master stability functions for synchronized coupled systems. *Phys. Rev. Lett.*, 80(10):2109–2112, 1998.

[95] B. Ravoori. *Synchronization of Chaotic Optoelectronic Oscillators Adaptive Techniques and the Design of Optimal Networks*. PhD thesis, University of Maryland, College Park, USA, 2011.

[96] H. Dao, J. C. Rodgers, R. Roy, and T. E. Murphy. Frequency-modulated time-delayed microwave chaotic oscillator. *IEICE*, invited paper, 2012.

[97] R. J. Sullivan. *Microwave Radar: Imaging and Advanced Concepts*. Artech Print, first edition, 2000.

[98] L. M. Pecora and T. L. Carroll. Synchronization in chaotic systems. *Phys. Rev. Lett.*, 64(8):821–824, 1990.

[99] H. Wu. Adaptive stabilizing state feedback controllers of uncertain dynamical systems with multiple time delays. *Automatic Control, IEEE Transactions on*, 45(9):1697–1701, 2000.

[100] A. Ahlborn and U. Parlitz. Stabilizing unstable steady states using multiple delay feedback control. *Phys. Rev. Lett.*, 93:264101, 2004.

[101] T. Jüngling, A. Gjurchinovski, and V. Urumov. Experimental time-delayed feedback control with variable and distributed delays. *Phys. Rev. E*, 86:046213, 2012.

[102] A. Gjurchinovski and V. Urumov. Variable-delay feedback control of unstable steady states in retarded time-delayed systems. *Phys. Rev. E*, 81:016209, 2010.

[103] A. Gjurchinovski and V. Urumov. Stabilization of unstable steady states by variable-delay feedback control. *EPL (Europhysics Letters)*, 84(4):40013, 2008.

[104] T. Dahms, P. Hövel, and E. Schöll. Control of unstable steady states by extended time-delayed feedback. *Phys. Rev. E*, 76:056201, 2007.

[105] J. E. S. Socolar, D. W. Sukow, and D. J. Gauthier. Stabilizing unstable periodic orbits in fast dynamical systems. *Phys. Rev. E*, 50:3245–3248, 1994.